



Master's Thesis

Search for Light Sterile Neutrinos with the KATRIN Experiment

Xaver Stribl

November 30th, 2022

Reviewer: Prof. Dr. Susanne Mertens
Second reviewer: Dr. Thierry Lasserre

Declaration of Authorship

I hereby declare that I have written this Master's Thesis independently and only with the use of the cited resources.

Erklärung der Selbstständigkeit

Ich versichere hiermit, dass ich die vorliegende Masterarbeit selbstständig verfasst und keine anderen als die angegebenen Quellen und Hilfsmittel benutzt habe.

Xaver Stribl
Munich, November 30th, 2022

Abstract

Sterile neutrinos do not participate in the weak interaction and are present in most extensions of the standard model of particle physics. Light sterile neutrinos with a mass on the eV-scale could explain several anomalies observed in short-baseline oscillation experiments.

The Karlsruhe Tritium Neutrino (KATRIN) experiment is designed to directly determine the effective electron anti-neutrino mass by measuring the tritium beta decay spectrum in the close vicinity of the endpoint, where the neutrino mass manifests itself as a small spectral distortion. The data can also be used to search for the signature of light sterile neutrinos. These would lead to a kink-like signature further away from the endpoint. Subsequently, exclusion limits on the active-to-sterile mixing $|U_{e4}|^2$ and the squared mass m_4^2 can be set.

The detector of the KATRIN experiment consists of 148 pixels, which are combined into 14 so-called patches. Moreover, the data is divided into multiple measurement campaigns. For the analysis, each data set is described by its own model, which makes the analysis computationally challenging. For the standard neutrino mass analysis this challenge is solved by applying a neural network for the model evaluation.

In this work, two approaches to solve the computational challenge are investigated: the adaptation of the neural network for the light sterile neutrino analysis and a simplification of the analysis via the averaging of multiple data sets.

For the former, the software is extended and multiple validation tests are performed. The applicability of the neural network to the light sterile neutrino analysis is demonstrated. For the latter, the combination of multiple detector patches into so-called pseudo-patches is investigated, illustrating that four pseudo-patches would be sufficient for the analysis.

A major part of this thesis is the application of the neural network to study the sensitivity of the first five measurement campaigns of the KATRIN experiment and check the impact of individual systematic uncertainties. As the data is not yet unblinded, the analysis is performed on a Monte-Carlo copy of the data. The resulting sensitivity shows that important parts of the light sterile neutrino parameter space could be excluded with the data from the first five measurement campaigns. These include the part of the gallium anomaly currently not excluded by oscillation experiments as well as almost all of the parameter space corresponding to the claimed observation of the Neutrino-4 experiment.

Contents

1	Neutrino Physics	1
1.1	Postulation and Discovery	1
1.2	Neutrino Oscillations	2
1.3	Neutrino Mass Determination	4
1.3.1	Cosmology	4
1.3.2	Neutrinoless Double Beta Decay	4
1.3.3	Kinematics of Beta Decay	4
1.4	Light Sterile Neutrinos	6
1.4.1	Search for Light Sterile Neutrinos	6
1.4.2	Light Sterile Neutrino Anomalies	7
2	The KATRIN Experiment	11
2.1	Experimental Setup	11
2.1.1	Rear Section	11
2.1.2	Windowless Gaseous Tritium Source	11
2.1.3	Transport Section	12
2.1.4	Spectrometer Section	12
2.1.5	Focal Plane Detector	14
2.2	Model of the Spectrum	15
2.2.1	Differential Energy Spectrum of Molecular Tritium Decay	15
2.2.2	Response Function	16
2.2.3	Integral Spectrum and Expected Count Rate	17
2.3	Systematic Effects	18
3	Analysis Strategy	21
3.1	Software	21
3.1.1	Fitrium	21
3.1.2	Netrium	21
3.2	Statistical Methods	22
3.2.1	Maximum Likelihood Analysis	22
3.2.2	Grid Scan	23
3.2.3	Raster Scan	23
3.3	Data Combination	24
3.3.1	Combination of Pixels	24
3.3.2	Combination of Runs	24
3.3.3	Combination of Measurement Campaigns	24
4	Netrium for the Light Sterile Neutrino Analysis	25
4.1	Light Sterile Neutrino Signal	25
4.2	Individual Fits	26
4.3	Sensitivity Contours	28

5 Pixel Combination for the Light Sterile Neutrino Analysis	31
5.1 Pixel Combinations	31
5.2 Impact of the Pixel Combination for the Null Hypothesis	32
5.3 Impact of the Pixel Combination with a Sterile Neutrino Signal	33
6 Sensitivity of the First Five Measurement Campaigns	37
6.1 Individual and Combined Sensitivity	37
6.2 Systematic Uncertainties	39
6.3 Comparison with Other Experiments	43
6.4 Extended Fit Range	44
7 Conclusion	47
A Systematic Uncertainties of All Measurement Campaigns	49
List of Acronyms	57
List of Figures	59
List of Tables	61
Bibliography	63
Acknowledgements	67

Chapter 1

Neutrino Physics

Originally postulated as an emergency solution to explain contradictory observations almost a century ago, the neutrino and the determination of its properties remains of major interest for particle physics and cosmology. The observation of neutrino oscillations has shown that neutrinos are not massless and therefore offered the first experimental evidence that the standard model of particle physics (SM) is incomplete. Determining the neutrino mass as well as the search for new particles, called sterile neutrinos, is actively pursued by experiments. Throughout this thesis, natural units ($\hbar = c = 1$) are used.

1.1 Postulation and Discovery

The existence of the neutrino was postulated in 1930 by Wolfgang Pauli to explain the observed energy spectrum of beta decay electrons [1]. Contrary to the expectation of a sharp peak centered around the endpoint energy of the decay, a continuous spectrum was observed (see Figure 1.1), which seemed to violate conservation laws and could not be explained by a two-body decay. Pauli proposed a new, electrically neutral, spin- $\frac{1}{2}$ particle to be emitted together with the electron in the decay. The energy would then be shared between these two particles and the daughter nucleus, resulting in a continuous energy spectrum. Due to its weak interaction with matter, the existence of the neutrino was only experimentally confirmed in 1956. The project poltergeist, lead by C. L. Cowan and F. Reines, was located near the Savannah River Plant nuclear reactor and employed a liquid scintillator for γ -ray detection as well as a tank containing a solution of cadmium chloride in water. The emitted electron anti-neutrinos undergo inverse beta decay with the protons in the liquid scintillator,

$$\bar{\nu}_e + p \rightarrow e^+ + n. \quad (1.1)$$

The resulting positron annihilates with surrounding electrons, releasing two γ -rays. With some time delay the neutron is captured by the cadmium, releasing a single γ -ray. Subsequently, the scintillation light produced by these γ -rays is detected. The measured signal of two coincidental peaks with some time delay could then be identified as induced by an electron anti-neutrino [2]. In 1962, the Brookhaven experiment measured muon neutrinos ν_μ for the first time [3], and in 2000 the DONUT experiment provided evidence for the existence of the tau neutrino ν_τ [4].

These observations have shown that there is one neutrino for every type of lepton, called the lepton flavor. In the SM, this is described by three leptonic families,

$$\begin{pmatrix} \nu_e \\ e^- \end{pmatrix}, \begin{pmatrix} \nu_\mu \\ \mu^- \end{pmatrix}, \begin{pmatrix} \nu_\tau \\ \tau^- \end{pmatrix}; \quad (1.2)$$

with the charged leptons of charge $q = -e$ and the neutral neutrinos. The neutrinos are further assumed to be massless in this description [5].

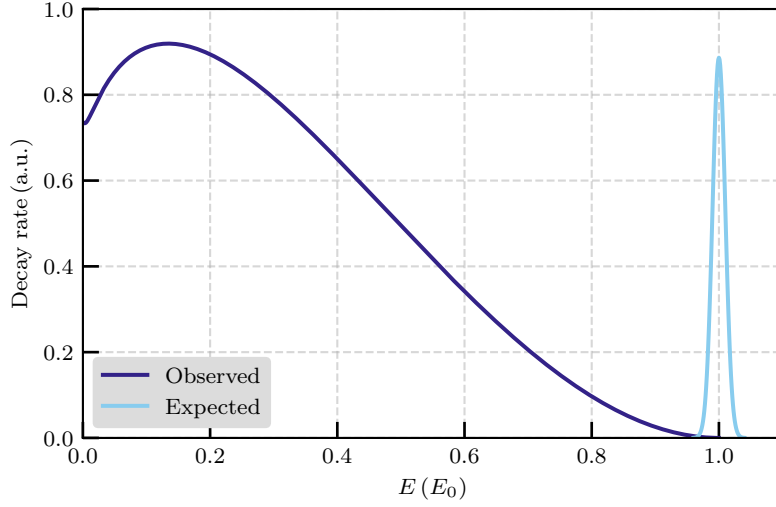


Figure 1.1: Sketch of the observed energy spectrum of beta decay electrons in comparison to the expected spectrum. The continuous spectrum cannot be explained by a two-body but a three-body decay.

1.2 Neutrino Oscillations

In 1968, the Homestake experiment measured the flux of electron neutrinos from ${}^8\text{B}$ decay in the sun. The observed flux was smaller than what was expected, which became known as the solar neutrino problem [6]. Pontecorvo had already brought up the idea of neutrino–anti-neutrino oscillations in 1958 [7] and in 1962 Maki, Nagakawa and Sakata introduced the possibility of neutrino flavor oscillations [8]. Pontecorvo also anticipated the solar neutrino problem in 1967 [9], shortly before its observation.

Neutrinos are produced and detected in their flavor eigenstates $|\nu_\alpha\rangle$; $\alpha \in \{e, \mu, \tau\}$ in weak charged current interactions. These states are not identical to the eigenstates of the Hamiltonian of the free particles $|\nu_i\rangle$; $i \in \{1, 2, 3\}$, which have a defined mass m_i . The flavor eigenstates can be viewed as a linear superposition of the mass eigenstates,

$$|\nu_\alpha\rangle = \sum_{i=1}^3 U_{\alpha i} |\nu_i\rangle, \quad (1.3)$$

where $U_{\alpha i}$ are the elements of the Pontecorvo-Maki-Nakagawa-Sakata (PMNS) matrix. Even though neutrinos interact in their flavor eigenstates, they propagate through time and space in their mass eigenstates. If the neutrinos have masses m_i with small differences, this can lead to a macroscopic effect where they periodically change their flavor [10, 5, 11].

To better understand this concept, it is common to look at the simplified case of only two neutrinos with $\alpha \in \{e, \mu\}$ and $i \in \{1, 2\}$. The PMNS matrix can then be written as the rotation matrix in two dimensions and Equation 1.3 as

$$\begin{pmatrix} |\nu_e\rangle \\ |\nu_\mu\rangle \end{pmatrix} = \begin{pmatrix} \cos(\theta) & \sin(\theta) \\ -\sin(\theta) & \cos(\theta) \end{pmatrix} \cdot \begin{pmatrix} |\nu_1\rangle \\ |\nu_2\rangle \end{pmatrix}. \quad (1.4)$$

The time evolution of the mass eigenstates is described by

$$|\nu_i(t)\rangle = \exp(-iE_i t) |\nu_i(0)\rangle, \quad (1.5)$$

where $E_i = \sqrt{\mathbf{p}_i^2 + m_i^2}$ are the energy eigenvalues of the mass eigenstates with \mathbf{p}_i the spatial momentum the neutrino is produced with. Assuming an electron neutrino is produced in a weak charged current interaction at $t = 0$, the state will evolve in time according to

$$|\nu_e(t)\rangle = \exp(-iE_1t) \cos(\theta) |\nu_1\rangle + \exp(-iE_2t) \sin(\theta) |\nu_2\rangle. \quad (1.6)$$

Using Taylor expansion for highly relativistic neutrinos, the energy can be estimated by $E_i \simeq |\mathbf{p}| + m_i^2/2|\mathbf{p}|$, also using $|\mathbf{p}| = |\mathbf{p}_i|$, since $|\mathbf{p}_i| \simeq |\mathbf{p}_j| \forall i, j$. The probability to still observe an electron neutrino after some time t is then given as

$$P_{\nu_e \rightarrow \nu_e} = |\langle \nu_e(t) | \nu_e \rangle|^2 = 1 - \sin^2(2\theta) \sin^2\left(\frac{\Delta m_{21}^2 L}{4|\mathbf{p}|}\right), \quad (1.7)$$

with $\Delta m_{21}^2 := m_2^2 - m_1^2$ the difference of the squared masses and L the distance the neutrino has travelled in the time t . The probability to find a muon neutrino is

$$P_{\nu_e \rightarrow \nu_\mu} = 1 - P_{\nu_e \rightarrow \nu_e} = \sin^2(2\theta) \sin^2\left(\frac{\Delta m_{21}^2 L}{4|\mathbf{p}|}\right). \quad (1.8)$$

These relations show that the probabilities oscillate as a function of $L/|\mathbf{p}|$ and that it is not certain that the neutrino will be detected in the same flavor it was produced, if the following conditions hold:

$$\theta \neq 0 \text{ and } \theta \neq \frac{\pi}{2}, \quad (1.9)$$

$$\Delta m_{21}^2 = m_2^2 - m_1^2 \neq 0. \quad (1.10)$$

Condition 1.10 is only fulfilled if the masses m_1 and m_2 are not equal and at most one of them is equal to zero.

For the real case of three neutrino generations, $\alpha \in \{e, \mu, \tau\}$, constraint 1.9 has to be fulfilled for all mixing angles and the additional constraints on the difference of the squared masses are

$$\Delta m_{31}^2 = m_3^2 - m_1^2 \neq 0, \quad (1.11)$$

$$\Delta m_{32}^2 = m_3^2 - m_2^2 \neq 0. \quad (1.12)$$

Like in the two neutrino scenario, the conditions 1.10, 1.11 and 1.12 are fulfilled if all three masses are different and at most one of them is equal to zero [10, 5, 11]. An observation of neutrino oscillations would therefore prove that neutrinos are massive, contradictory to their description in the SM.

In 1998, experimental evidence for neutrino oscillations was provided by the Super-Kamiokande experiment, by measuring the atmospheric neutrino flux. While the measured number of electron neutrinos did not deviate significantly from expectations, the observed ratio of muon to electron neutrinos did. Therefore, it was concluded that the muon neutrinos change their flavor to tau neutrinos and that these measurements give evidence for neutrino oscillations [12].

Three years later, the Sudbury Neutrino Observatory (SNO) published results further confirming these observations. The SNO measured solar neutrinos from ${}^8\text{B}$ decay and found a deficiency in the flux of electron neutrinos in comparison to the total neutrino flux. This led to the conclusion that not all observed solar neutrinos are electron neutrinos and that some of the ${}^8\text{B}$ electron neutrinos change their flavor [13]. In a follow-up SNO publication, it was observed that the total flux is made up of equal parts of all three flavors, thus resolving the solar neutrino problem [14].

The observation of neutrino oscillations has shown that neutrinos periodically change their flavor and that neutrinos must be massive particles. However, from oscillation experiments only the mixing angles $\theta_{\alpha i}$ and the splittings between the three masses Δm_{ij}^2 can be determined. What remains unknown is the sign of Δm_{31}^2 , which defines the mass hierarchy, as well as the absolute mass scale. Ways to determine the neutrino masses are discussed in the next section.

1.3 Neutrino Mass Determination

The determination of the neutrino mass is of great interest, since the mechanism of neutrino mass creation as well as the absolute mass scale remain unknown. Neutrinos further play an important role in the formation of large scale structures in the universe, and the knowledge of the neutrino mass would provide an important input to cosmological models [15]. In the following, the three main approaches to determining the neutrino mass are discussed.

1.3.1 Cosmology

With a number density of 339 relic neutrinos and anti-neutrinos per cm^3 , neutrinos are the second most abundant particle in the universe and therefore play an important role in its evolution. From cosmological measurements the neutrino energy density Ω_ν can be determined, which directly depends on the sum of all neutrino masses [16],

$$m_\Sigma = \sum_i m_i. \quad (1.13)$$

The current upper limits at 95% confidence level (C.L.) range from $m_\Sigma \leq 0.087 \text{ eV}$ to $m_\Sigma \leq 0.54 \text{ eV}$ [17], strongly depending on the used model and data.

1.3.2 Neutrinoless Double Beta Decay

Another way to determine the neutrino mass would be the observation of neutrinoless double beta decay ($0\nu\beta\beta$). Normal double beta decay ($2\nu\beta\beta$) is the rarest nuclear weak process, where two neutrons decay simultaneously into two protons under emission of two electrons and two electron anti-neutrinos,

$$(Z, A) \rightarrow (Z + 2, A) + 2e^- + 2\bar{\nu}_e, \quad (1.14)$$

where Z is the atomic charge and A the atomic number. If neutrinos are Majorana particles and therefore their own anti-particles, $0\nu\beta\beta$ would be possible. The two neutrinos would not be emitted,

$$(Z, A) \rightarrow (Z + 2, A) + 2e^-, \quad (1.15)$$

and the decay would therefore violate lepton number conservation [18].

The experimental signature of $0\nu\beta\beta$ is a small peak at the endpoint of the $2\nu\beta\beta$ energy spectrum, since the two electrons share almost all of the energy. Experiments can determine the decay rate $\Gamma_{0\nu\beta\beta}$, which is proportional to the effective majorana mass

$$\langle m_{\beta\beta} \rangle = \left| \sum_i U_{ei}^2 m_i \right|. \quad (1.16)$$

Note that $\langle m_{\beta\beta} \rangle$ is the coherent sum of the neutrino masses, where the matrix element U_{ei}^2 contains unknown CP -violating Majorana phases, which can lead to cancelations in the sum. Therefore, $\langle m_{\beta\beta} \rangle$ could be smaller than each m_i [19].

To this day, $0\nu\beta\beta$ has not been observed, but upper limits on $\langle m_{\beta\beta} \rangle$ have been set. Current limits at 90% C.L. are provided by GERDA with $\langle m_{\beta\beta} \rangle < (0.079 - 0.180) \text{ eV}$ [20] and KamLAND-Zen with $\langle m_{\beta\beta} \rangle < (0.036 - 0.156) \text{ eV}$ [21]. These limits are however only valid if neutrinos are Majorana particles.

1.3.3 Kinematics of Beta Decay

In contrast to the two methods described above, the kinematics of single beta decay provide a model independent method to probe the absolute neutrino mass scale. In beta decay, a neutron

decays into a proton under emission of an electron and an electron anti-neutrino,

$$(Z, A) \rightarrow (Z + 1, A) + e^- + \bar{\nu}_e. \quad (1.17)$$

The surplus energy Q is shared between the kinetic energy of the electron E , the total energy of the neutrino E_ν and the recoil energy on the daughter nucleus E_{rec} [22, 23]. The endpoint energy is then

$$E_0 = Q - E_{\text{rec}} = E + E_\nu, \quad (1.18)$$

which shows that the maximum energy the electron can have is

$$E_{\text{max}} = E_0 - m_\nu, \quad (1.19)$$

i.e. the difference of the endpoint energy and the effective electron anti-neutrino mass,

$$m_\nu = \sqrt{\sum_i |U_{ei}|^2 m_i^2}, \quad (1.20)$$

which is the incoherent sum of the neutrino masses. The differential decay rate is described by Fermi's theory for beta decay as

$$\frac{d\Gamma}{dE}(E, m_\nu^2) = \frac{G_F^2 \cos^2(\theta_C)}{2\pi^3} \cdot |M_{\text{nuc}}|^2 \cdot F(Z, E) \cdot p(E + m_e) \cdot E_\nu \sqrt{E_\nu^2 - m_\nu^2} \cdot \Theta(E_\nu - m_\nu), \quad (1.21)$$

with

G_F : Fermi constant,	m_e : Mass of the electron,
θ_C : Cabibbo angle,	E_ν : Total energy of the neutrino,
M_{nuc} : Nuclear matrix element,	m_ν : Effective electron anti-neutrino mass (see Equation 1.20),
F : Fermi function with atomic charge Z ,	Θ : Heaviside step-function.
p : Momentum of the outgoing electron,	
E : Kinetic energy of the electron,	

The full differential beta decay spectrum for tritium with $F(Z = 2, E)$ is shown in Figure 1.2 (left). The differential decay rate (Equation 1.21) is affected by m_ν^2 in the phase space factor of the neutrino, $E_\nu \sqrt{E_\nu^2 - m_\nu^2}$. This leads to a signature of the neutrino mass in the energy spectrum close to the endpoint [23, 24], as shown in Figure 1.2 (right) for the beta decay of tritium.

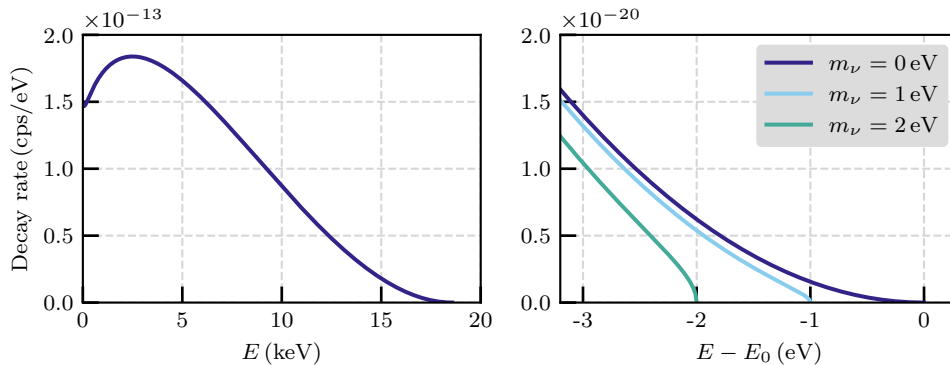


Figure 1.2: Impact of m_ν on the tritium beta spectrum. **Left:** Full energy spectrum of tritium beta decay with $F(Z = 2, E)$. **Right:** Zoom-in on the endpoint of the energy spectrum with different values of m_ν .

To infer m_ν from the kinematics of beta decay, one has to measure the region of the spectrum with low energy neutrinos, ideally E_{\max} (see Equation 1.19), which corresponds to the small part very close to the endpoint of the energy spectrum. Therefore, it is common to choose beta-emitters with a low endpoint energy. The usual choice is tritium, because of its short half life of 12.3 years and low endpoint energy of about 18.6 keV [22]. Currently, the best limit on m_ν is provided by the KATRIN experiment, with $m_\nu < 0.8$ eV at 90% C.L. [15]. The KATRIN experiment and its use of molecular tritium will be discussed in more detail in the next chapter.

1.4 Light Sterile Neutrinos

While results from the Large Electron-Positron collider regarding the decay of the Z boson show that there are only three light neutrinos that take part in the weak interaction, several anomalies in neutrino experiments (as reviewed in 1.4.2) could be explained by the existence of additional neutrino flavors that do not interact weakly. These sterile neutrinos are also present in most extensions of the SM. The simplest case is that of an additional heavy fourth mass eigenstate ν_4 , with mass $m_4 \gtrsim 1$ eV, that has a very small mixing with the active neutrinos and a large mixing with a sterile neutrino flavor eigenstate ν_s . This is often called the $(3+1)\nu$ model as compared to the standard 3ν model. The PMNS matrix would extend to a 4×4 matrix and Equation 1.3 would describe the flavor eigenstates as superpositions of the mass eigenstates with $\alpha \in \{e, \mu, \tau, s\}$ and $i \in \{1, 2, 3, 4\}$ [25, 26].

1.4.1 Search for Light Sterile Neutrinos

Oscillation Experiments

In the framework of the $(3+1)\nu$ model, the three active neutrinos mix with the sterile neutrino. With $m_4 \gtrsim 1$ eV and therefore

$$m_4 \gg m_i; \quad i \in \{1, 2, 3\}, \quad (1.22)$$

$$\Delta m_{41}^2 \approx \Delta m_{42}^2 \approx \Delta m_{43}^2, \quad (1.23)$$

$$\Delta m_{41}^2 \gg \Delta m_{21}^2, \Delta m_{41}^2 \gg \Delta m_{32}^2, \quad (1.24)$$

the mixing would be observable for experimental configurations with $4|\mathbf{p}| \sim \Delta m_{4i}^2 L$, where the active oscillations are not relevant. Thus, the active-to-sterile mixing can be described in the two-neutrino approximation:

$$P_{\nu_\alpha \rightarrow \nu_\beta} = \left| \delta_{\alpha\beta} - \sin^2(2\theta_{\alpha\beta}) \sin^2\left(\frac{\Delta m_{4i}^2 L}{4|\mathbf{p}|}\right) \right|. \quad (1.25)$$

In general, oscillation experiments are sensitive to the mass splittings Δm_{4i}^2 and the mixing amplitudes,

$$\sin^2(2\theta_{\alpha\beta}) = 4 |U_{\alpha 4}|^2 \left| \delta_{\alpha\beta} - |U_{\beta 4}|^2 \right|, \quad (1.26)$$

depending on the observed neutrino flavor. The two main approaches for the search for light sterile neutrinos with oscillation experiments are appearance and disappearance searches. The current anomalies from short-baseline oscillation experiments (as discussed in the next section, 1.4.2) regard the disappearance of electron neutrinos and anti-neutrinos [25]. These experiments are sensitive to the mass splitting Δm_{41}^2 and the mixing amplitude for $\nu_e \rightarrow \nu_e$,

$$\sin^2(2\theta_{ee}) = 4 |U_{e4}|^2 \left(1 - |U_{e4}|^2 \right) = \sin^2(2\theta_{14}). \quad (1.27)$$

Kinematics of Beta Decay

As discussed before, the electron neutrino produced in beta decay is a superposition of the mass eigenstates, and hence the beta spectrum is a superposition of three spectra corresponding to the

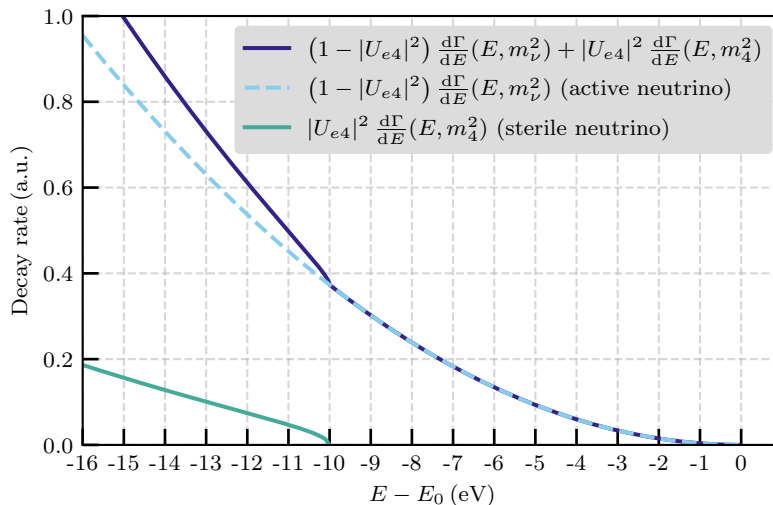


Figure 1.3: Impact of a light sterile neutrino with $m_4^2 = (10 \text{ eV})^2$ and $|U_{e4}|^2 = 0.2$ on the energy spectrum of tritium beta decay with $m_\nu^2 = 0 \text{ eV}^2$ and $F(Z = 2, E)$.

different masses m_i ; $i \in \{1, 2, 3\}$. Because the difference between these masses is so small, it cannot be resolved by the KATRIN experiment. Since $m_4 \gg m_i$ however, the sterile decay branch could be resolved and the decay spectrum can be described as a superposition of the active and the sterile branch:

$$\frac{d\Gamma}{dE}(E, m_\nu^2, m_4^2, |U_{e4}|^2) = (1 - |U_{e4}|^2) \frac{d\Gamma}{dE}(E, m_\nu^2) + |U_{e4}|^2 \frac{d\Gamma}{dE}(E, m_4^2). \quad (1.28)$$

The decay branch of the sterile neutrino would show as a characteristic distortion of the spectrum at $E = E_0 - m_4$, often called “kink” [25]. The impact of a sterile neutrino on the beta spectrum of tritium is shown in Figure 1.3. Experiments investigating the kinematics of beta decay are sensitive to the squared mass of the sterile neutrino m_4^2 and the active-to-sterile mixing $|U_{e4}|^2 = \sin^2(\theta_{14})$. With $\Delta m_{41}^2 \approx m_4^2$ (since $m_4 \gg m_i$) and Equation 1.27, the constraints on the sterile parameters from beta decay experiments can be compared to short-baseline electron (anti-)neutrino disappearance experiments.

1.4.2 Light Sterile Neutrino Anomalies

There are several results from neutrino oscillation experiments that are not fully understood. These results can, in principle, separately be explained by the existence of light sterile neutrinos, while not necessarily consistent with each other. However, none of these observations provide any clear evidence for light sterile neutrinos. The most prominent results are briefly discussed in this section, with a synthesis and an assessment of the current situation at the end.

Gallium Anomaly

In calibration measurements of the solar neutrino experiments GALLEX and SAGE, a deficit in the measured neutrino rate compared to the expected rate was observed [27, 28]. The average ratio of the measured rate to the expected rate is 0.84 ± 0.05 at 2.9σ [29], which is known as the gallium anomaly (GA), since both experiments use the inverse beta decay on ${}^{71}\text{Ga}$ as the detection process [25]. The result can be explained by a light sterile neutrino with $\sin^2(2\theta_{14}) \gtrsim 0.14 - 0.23$ at 2σ for $\Delta m_4^2 \gtrsim 0.6 \text{ eV}^2$, depending on the model for the cross section.

The Baksan Experiment on Sterile Transitions (BEST), specifically designed to investigate the

rate deficit observed in previous gallium experiments, published its results very recently. It deployed two ^{71}Ga targets at two different distances from the source, to also take possible rate differences caused by the oscillation length into account. The observed rates are $R_{\text{out}} = 0.77 \pm 0.05$ and $R_{\text{in}} = 0.79 \pm 0.05$, so no significant difference between the rate in the inner and outer target is observed [30]. However, the large deviance from unity in both rates makes the GA more pronounced with a weighted average ratio of expected to measured rate for all gallium experiments of 0.80 ± 0.05 [31].

Reactor Anti-Neutrino Anomaly

The reactor anti-neutrino anomaly (RAA) refers to the deficit in electron anti-neutrino flux observed in short-baseline ($L < 100$ m) reactor neutrino experiments. In 2011, the predictions of the expected rates for reactor anti-neutrinos were improved [32]. A re-evaluation of these experiments, in light of these new predicted rates, has shown that the measured neutrino flux is smaller than expected, with a ratio of measured to expected event rates of 0.943 ± 0.023 at 98.6% C.L. [33]. Like for the GA, this anomaly can be explained by a light sterile neutrino with $\sin^2(\theta_{14}) \lesssim 0.14 - 0.25$ at 2σ for $\Delta m_4^2 \gtrsim 2 \text{eV}^2$ [34], depending on the model, but also by a false prediction of the anti-neutrino flux from nuclear reactors.

An updated model provided by Estienne, Fallot *et al.* (EF model) leads to a significantly better agreement between the observed and expected neutrino flux [35], although with large uncertainties. In 2021, measurements at a research reactor at the National Research Centre Kurchatov Institute (KI) were used to re-evaluate the ratio of the ^{235}U to the ^{239}Pu electron spectrum from nuclear reactors, since these isotopes are the primary source for reactor neutrinos. The observations suggest that the normalizations of spectra may have been overestimated before, which would also significantly reduce the discrepancy between the measured and expected anti-neutrino flux in short-baseline oscillation experiments [36]. With these new models, the ratio of the measured to predicted event rates deviates only about 1σ from unity [31]. As already mentioned, the primary source for reactor neutrinos are ^{235}U and ^{239}Pu decays. When comparing the flux from the model to the data, it is found that it is in agreement for the flux from ^{239}Pu fissions, but not for ^{235}U fissions, where the measured value is lower than the expected value [37]. In the case of light sterile neutrinos, one would expect that the deficit is present independently of the fission isotope.

Neutrino-4

The Neutrino-4 collaboration is measuring the anti-neutrino flux of a nuclear reactor on a very short baseline (6 – 12 m). They claim to observe a sterile neutrino with $\Delta m_{41}^2 = (7.3 \pm 1.17) \text{eV}^2$ and $\sin^2(2\theta_{14}) = 0.36 \pm 0.12$ at 2.9σ [38]. This result is controversially discussed by the community.

It has been pointed out that the energy resolution of the detector is neglected in the analysis, which strongly effects the results and their significance [39, 40]. Further, it was shown that using a more reliable Monte Carlo method instead of Wilk's theorem decreases the statistical significance [39]. Also the signal-to-background ratio is quoted as 0.52 [38], which is lower than in most competitor experiments.

Synthesis and Current Status of Light Sterile Neutrinos

With the new results from BEST, the GA is more pronounced than before. As mentioned above, the GA can be explained by a light sterile neutrino. However, the data from GALLEX, SAGE and BEST show no clear $\nu_e \rightarrow \nu_s$ oscillation pattern and the rates observed by BEST at two different distances from the source are basically identical. Therefore, the GA provides no clear evidence for light sterile neutrinos [31].

Independent evidence, such as improved flux predictions and new measurements of the ratio of ^{235}U to ^{239}Pu electron spectra, shows that the origin of the RAA could lie in the prediction of the

reactor neutrino fluxes.

The limits on $\sin^2(2\theta_{14})$ from the GA are in tension with the ones from the RAA, as it can be seen in Figure 1.4, where the allowed regions from both anomalies cover distinct parts of the parameter space.

Both the GA and RAA are based on the comparison of the expected and measured neutrino flux, where the expected flux depends on the theoretical models for the cross section. To investigate short-baseline oscillations of reactor anti-neutrinos in a model-independent way, the rates at different distances from the source have to be measured. This approach is pursued by the DANSS [41], PROSPECT [42] and STEREO [43] experiments, which measure the spectrum at different distances. The results of these experiments are compatible with the no-oscillation hypothesis and are also in tension with the BEST and GA results [31], as they exclude most of the parameter space that would be needed to explain the GA with light sterile neutrinos (see Figure 1.4).

Another experiment that measures the rates at different distances from the reactor is Neutrino-4. The Neutrino-4 result, especially the claim of an observation, is in strong tension with the results from PROSPECT and STEREO. While the observed oscillatory pattern raises some questions, its significance is questionable and several problems in the analysis have been pointed out by the community, as discussed above. Furthermore, the signal to background ratio is very low and the result should be confirmed with an improved setup. In light of all this, the claim of an observation may not be justified.

The current results from short-baseline oscillation experiments are not conclusive, but they do not clearly point towards the existence of light sterile neutrinos. With the RAA on the way to being solved and the Neutrino-4 result excluded by other experiments, what remains is the GA. While a large part of the allowed parameter space from the BEST and GA results is already excluded, there is still some part uncovered by other experiments, indicated by the red shaded area in Figure 1.4. The KATRIN experiment has the potential to cover this part of the parameter space, as shown in Figure 1.4. As the search for light sterile neutrinos with the KATRIN experiment is the topic of this work, this is discussed in more detail in later Chapters. In particular the sensitivity on the previously discussed parameter space with the latest data is discussed in 6.3.

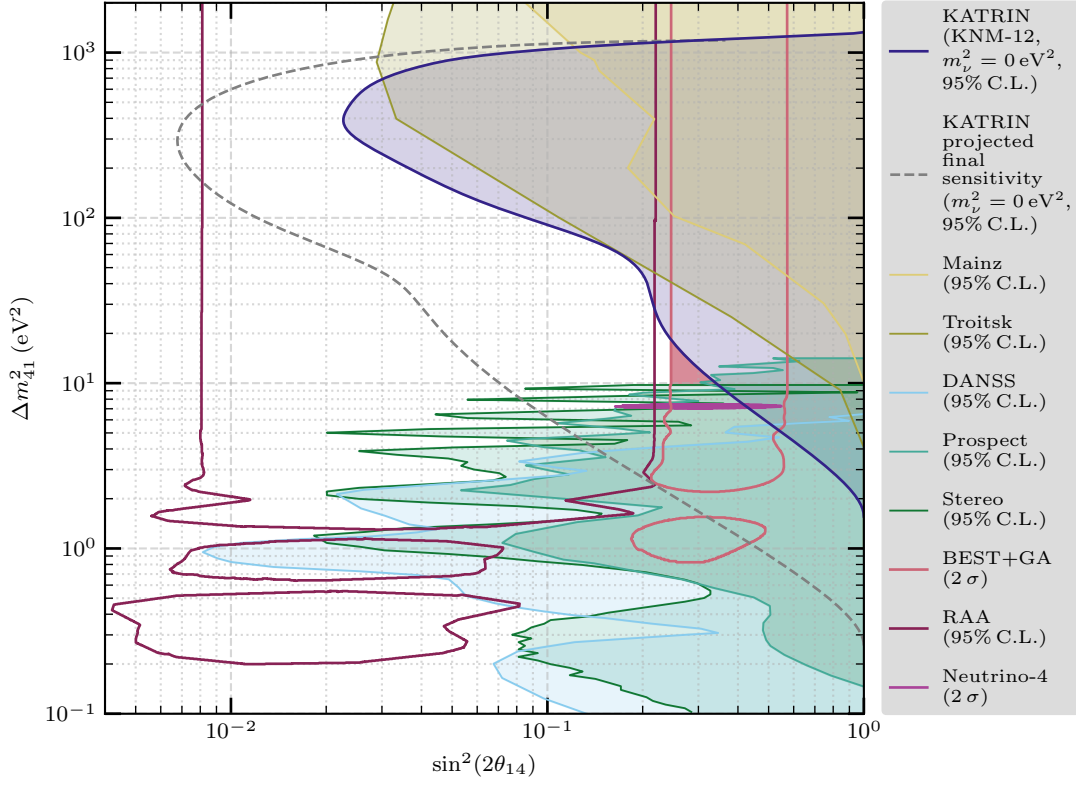


Figure 1.4: The current parameter space of light sterile neutrinos with restrictions from various experiments. For the BEST+GA, RAA and Neutrino-4 experiment the allowed part of the parameter space according to their respective results is shown. For the other experiments, the excluded part of the parameter space not allowed from their results is shown shaded. The parts of the parameter space allowed by the BEST+GA and RAA are in tension as they have no real overlap. The PROSPECT and STEREO experiments exclude the claimed observation of Neutrino-4. Also shown are the Mainz and Troitsk experiments, the predecessors of the KATRIN experiment. For the KATRIN experiment, the currently excluded part is shown as well as the projected final sensitivity, that could probe the majority of the BEST+GA parameter space. The part of the BEST+GA parameter space not excluded up to now is indicated by the shaded red area.

Chapter 2

The KATRIN Experiment

The Karlsruhe Tritium Neutrino (KATRIN) experiment is aiming to directly measure the effective electron anti-neutrino mass m_ν from beta decay of molecular tritium with a sensitivity of 0.2 eV at 90% C.L. It is the successor of the Mainz [44] and Troitsk [45] direct neutrino mass experiments and it allows the investigation of the sub-eV neutrino mass scale. In contrast to other methods of neutrino mass determination, such as cosmological observations or neutrinoless double beta decay, KATRIN provides a direct neutrino mass measurement, since its result is solely based on energy-momentum conservation and the kinematics of the decay [46].

2.1 Experimental Setup

The KATRIN experiment is located at the Forschungszentrum Karlsruhe, making use of the Tritium Laboratory Karlsruhe (TLK), which is equipped with a closed tritium cycle and is licensed to handle 40 g of tritium. The tritium source and other tritium related parts can thus be placed entirely in the TLK. The 70 m long experimental setup is shown in Figure 2.1 and made up of the following main parts [46]:

- Rear section (RS) (see 2.1.1),
- Windowless gaseous Tritium source (WGTS) (see 2.1.2),
- Transport Section with the differential pumping section (DPS) and the cryogenic pumping section (CPS) (see 2.1.3),
- Spectrometer Section with the pre-spectrometer (PS) and the main spectrometer (MS) (see 2.1.4),
- Detector system with the focal plane detector (FPD) (see 2.1.5),

which are discussed in more detail in the following sections.

2.1.1 Rear Section

The rear section (RS) contains two main components, the rear wall (RW) and an electron gun (e-gun). The RW is a disc with a gold surface that is placed at the front of the rear section, being the effective end of the windowless gaseous tritium source (WGTS). It is used to provide a constant and well-defined electric potential over the full WGTS [46, 47]. The purpose of the e-gun is to measure the transmission properties of the MS and to determine the energy loss of electrons due to elastic and inelastic scattering off tritium molecules in the WGTS [48, 49].

2.1.2 Windowless Gaseous Tritium Source

Since only a small fraction of $2 \cdot 10^{-13}$ of all beta decay electrons are in the region of 1 eV below the endpoint, a highly luminous source is needed. The 16 m long WGTS is designed to provide

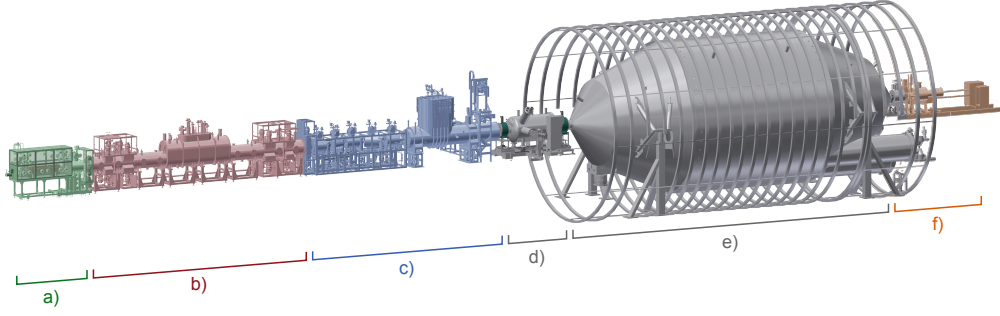


Figure 2.1: Overview of the experimental setup of the KATRIN experiment. **a)** Rear section (RS), **b)** Windowless gaseous tritium source (WGTS), **c)** Transport section with the differential pumping section (DPS) and the cryogenic pumping section (CPS), Spectrometer section with the **d)** Pre-spectrometer (PS) and the **e)** Main spectrometer (MS), **f)** Detector system with the focal plane detector (FPD). Figure provided by Leonard Köllenberger.

$9.5 \cdot 10^{10}$ beta decay electrons per second. It houses the inner beam tube with a diameter of 90 mm that is operated at a temperature of about 30 K in the first two measurement campaigns and at about 80 K afterwards. Molecular tritium (T_2) gas with an isotopic purity of over 95% is injected at the center and pumped out at both ends, with a nominal value for the column density of $5 \cdot 10^{17}$ Molecules/cm². The other main hydrogen isotopologues present in the source are DT and HT [46, 50].

2.1.3 Transport Section

While the WGTS is closed by the RW on one end, it is open on the other end towards the transport section, which serves the purpose of transporting the electrons from the source to the spectrometer section. The two main parts of the transport section are the DPS followed by the CPS, which reduce the tritium flow by 14 orders of magnitude [50].

The DPS contains four turbo-molecular pumps (TMPs) and five super-conducting magnets. To prevent a straight line of sight from the WGTS to the spectrometer section, the TMPs are inclined by 20° with respect to each other. The super-conducting magnets guide the electrons adiabatically from the source to the CPS, while a set of dipole and ring electrodes prevent positively charged ions from the source from passing through the DPS [51].

The final barrier of tritium circulation before the spectrometer section is the 7 m long CPS. Seven super-conducting magnets guide the electrons to the spectrometer section. The second and fourth magnets are inclined by 15° with respect to each other so that neutral tritium molecules hit the inner surface of the beamtube, where they are absorbed by a cryo pump, which is covered with a pre-condensed Argon frost layer [52, 53].

2.1.4 Spectrometer Section

After the transport section, the electrons reach the spectrometer section with the PS and the MS. Both of these spectrometers operate according to the MAC-E filter principle, applying magnetic adiabatic collimation in combination with an electrostatic filter. The working principle of the MAC-E filter principle is illustrated in Figure 2.2. An inhomogenous magnetic field is generated by two superconducting magnets, the source magnet at the beginning and the pinch magnet at the end of the spectrometer with a field strength of B_{src} and B_{max} , respectively. This field guides the electrons towards the center of the spectrometer, where the field strength drops several orders of magnitude. The electron has a transversal, E_{\perp} , and longitudinal, E_{\parallel} , energy component. Further, the electron carries out cyclotron motion around the magnetic field lines with a magnetic moment

consequently the PS is not operated anymore since the end of the fourth measurement campaign.

High energy electrons that pass the PS enter the MS, which is 23.3 m long and has a diameter of about 10 m. To minimize scattering effects, the MS is operated at an ultra-high vacuum of 10^{-11} mbar. In the MS, the electrons are analyzed for their kinetic energy, as described above. By varying the retarding potential, the endpoint region of the beta spectrum can be scanned by counting the amount of electrons for each retarding potential [46, 55].

As reaching a background rate of $\mathcal{O}(10)$ mcps, required for the design sensitivity of 0.2 eV at 95% C.L. within 3 years of measurement time, has proven to be difficult even after several improvements, additional measures to reduce the background are required. A method to reduce the background by a factor of two is the shifted analyzing plane (SAP) configuration. The basic idea is to reduce the effective volume of the flux tube in the MS and subsequently the background from Rydberg electrons [57]. This configuration has been tested in the first half of the third measurement campaign and is used permanently since the beginning of the fourth measurement campaign.

2.1.5 Focal Plane Detector

Electrons that pass the MS are post-accelerated towards the FPD, to increase the detection efficiency. The FPD is a multi-pixel silicon *p-i-n* diode detector with 148 pixels arranged in a dartboard pattern, each with an area of 44 mm^2 (see Figure 2.3). It has a detection efficiency of about 93% and a mean energy resolution of about 1.5 keV at full width half maximum [58].

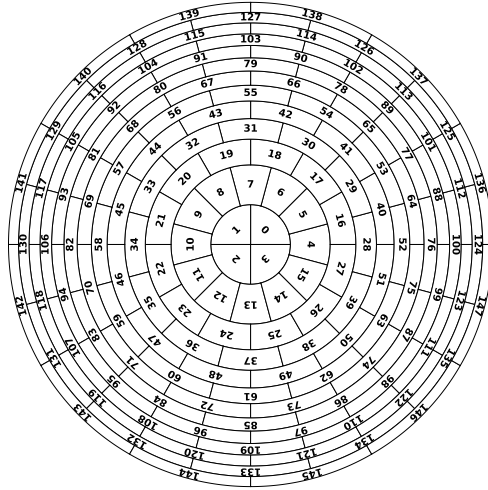


Figure 2.3: The FPD with 148 pixels, each with an area of 44 mm^2 , arranged in a dartboard pattern.

2.2 Model of the Spectrum

2.2.1 Differential Energy Spectrum of Molecular Tritium Decay

The KATRIN experiment uses the beta decay of molecular tritium,



The differential spectrum for atomic tritium is described in Section 1.3.3 by Equation 1.21 and shown in Figure 1.2. Several corrections have to be applied to obtain a model for the differential spectrum of molecular tritium and subsequently the integral spectrum that is actually measured.

After the decay, the daughter molecule $({}^3\text{HeT})^+$ is left in a rotational, vibrational or electronic excited final state f with energy V_f and probability P_f . Therefore, the neutrino energy has to be corrected by $E_\nu \rightarrow (E_\nu)_f = E_0 - V_f - E$. The differential decay rate, including the summation over all final states, is

$$\begin{aligned} \frac{d\Gamma}{dE}(E, m_\nu^2) &= \frac{G_F^2 \cos^2(\theta_C)}{2\pi^3} \cdot |M_{\text{nuc}}|^2 \cdot F(Z, E) \cdot p(E + m_e) \\ &\cdot \sum_f P_f (E_\nu)_f \sqrt{(E_\nu)_f^2 - m_\nu^2} \cdot \Theta((E_\nu)_f - m_\nu). \end{aligned} \quad (2.5)$$

Since the accuracy of a neutrino mass measurement depends strongly on the knowledge of the probability distribution of these final states, called the final state distribution (FSD), precise theoretical calculations are necessary. Additionally, the FSDs of the daughter molecules of the other hydrogen isotopologues present in the WGTS, DT and HT, as well as their respective concentration, have to be considered [24]. The FSD of $({}^3\text{HeT})^+$ is shown in Figure 2.4.

Further corrections arise from the Doppler shift caused by the thermal motion of the molecules in the WGTS and various theoretical corrections, for a more detailed description see [24].

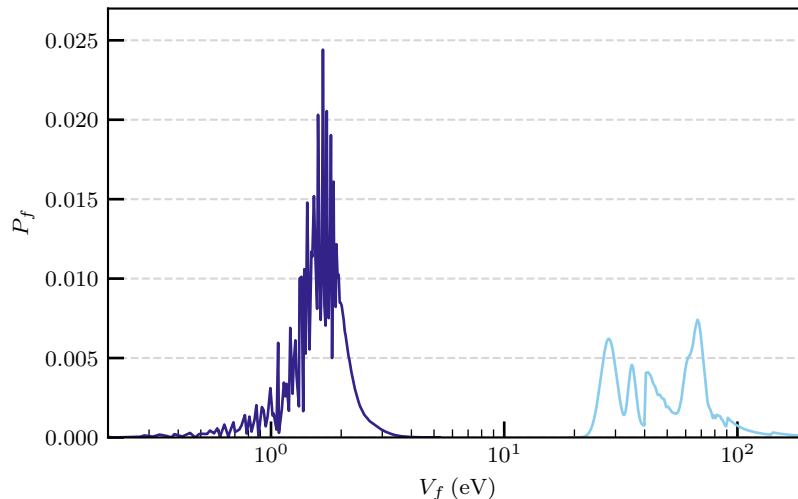


Figure 2.4: Final state distribution (FSD) of $({}^3\text{HeT})^+$ from T_2 decay. The left part (dark blue) corresponds to the rotational and vibrational final states, the right part (light blue) to the electronic excited final states.

2.2.2 Response Function

Another effect that has to be taken into account is the response function R of the experiment. It is determined by the probability that electrons pass the MAC-E filter for a given retarding potential, called the transmission function, and the energy lost by electrons in inelastic scattering with molecules in the source, which is described by the energy loss function.

The transmission function of the MAC-E filter for isotropically emitted electrons is analytically given by [46]

$$T(E; qU) = \begin{cases} 0 & \text{for } E - qU < 0, \\ \frac{1 - \sqrt{1 - \frac{E - qU}{E} \cdot \frac{B_{\text{src}}}{B_{\text{ana}}}}}{1 - \sqrt{1 - \frac{\Delta E}{E} \cdot \frac{B_{\text{src}}}{B_{\text{ana}}}}} & \text{for } 0 \leq E - qU \leq \Delta E, \\ 1 & \text{for } E - qU > \Delta E. \end{cases}$$

An example of a transmission function is shown in Figure 2.5 (left). Ideally the transmission function would be a step function at $E = qU$, but since the MAC-E filter has a finite resolution ΔE due to a remaining transversal energy component, electrons with energy $qU \leq E \leq qU + \Delta E$ have an energy dependent transmission probability.

However, interactions of electrons in the WGTS are not taken into account by the transmission function. Electrons that scatter inelastically with T_2 molecules lose energy, which impacts the response function. The mean probability to scatter i times in the whole source tube is given by

$$\bar{P}_i = \frac{1}{\rho d} \int_{-L/2}^{+L/2} \rho(z) \cdot \bar{P}_i(z) dz, \quad (2.6)$$

with ρd the total column density, L the length of the source, $\rho(z)$ the density profile of the source and $\bar{P}_i(z)$ the mean scattering probability at starting position z in the source [59]. The energy lost when scattering is described by the energy loss function $f(\epsilon)$ with ϵ the energy loss. It is parametrized by [48]

$$f(\epsilon) = \begin{cases} \sum_{j=1}^3 A_j \exp\left(-\frac{(\epsilon - \mu_j)^2}{2\sigma_j^2}\right) & \text{for } \epsilon \leq \epsilon_c, \\ \frac{f(\epsilon_c)}{f_{\text{BED}}(\epsilon_c)} \cdot f_{\text{BED}}(\epsilon) & \text{for } \epsilon > \epsilon_c, \end{cases}$$

where A_j , μ_j and σ_j are the amplitude, mean and standard distribution of three normal distributions and $f_{\text{BED}}(\epsilon)$ is the functional form of the binary-encounter-dipole (BED) model, which describes the ionization continuum. The normal distribution part for $\epsilon \leq \epsilon_c$ describes the energy lost due to excitation and the BED part for $\epsilon > \epsilon_c$ describes the energy lost due to ionization of

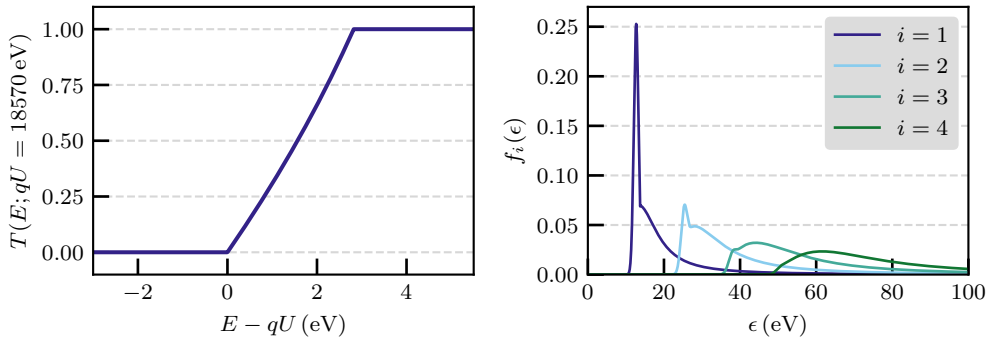


Figure 2.5: Left: Transmission function for $qU = 18570$ eV. **Right:** Energy loss function for one through four scatterings. The Gaussian parts correspond to the energy lost due to excitation and the BED parts to the energy lost due to ionization of tritium molecules.

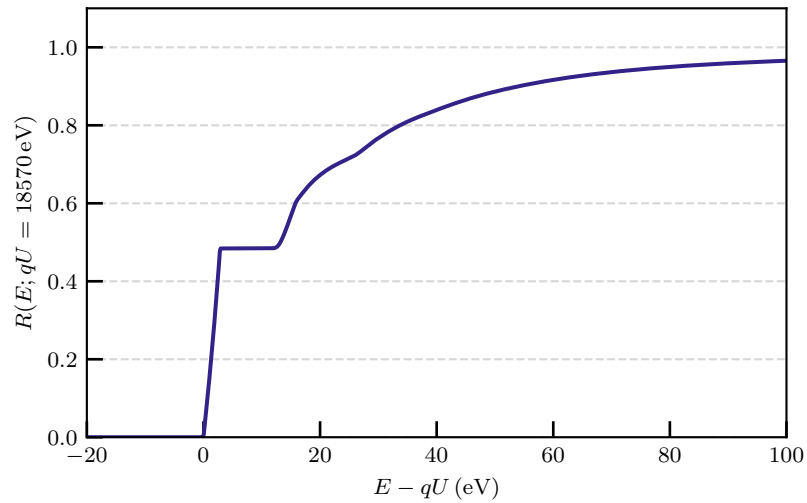


Figure 2.6: Response function for a maximum of $N = 7$ scatterings, $qU = 18570$ eV and 75% of the nominal column density.

tritium molecules. To get the energy loss function $f_i(\epsilon)$ for i scatterings, it is convolved i times with itself [59]. Figure 2.5 (right) shows the energy loss function for one through four scatterings.

The response function is then obtained by convolving the transmission function with the energy loss function weighted with the corresponding probability for N scatterings [59],

$$R(E; qU) = \int_{\epsilon=0}^{E-qU} T(E - \epsilon; qU) \cdot \sum_{i=0}^N \bar{P}_i f_i(\epsilon) d\epsilon, \quad (2.7)$$

which is shown in Figure 2.6 with a maximum of $N = 7$ scatterings, $qU = 18570$ eV and 75% of the nominal column density.

2.2.3 Integral Spectrum and Expected Count Rate

From the differential spectrum and the response function the integral spectrum can be calculated:

$$I(qU) = A \cdot \int_{qU}^{E_0} \frac{d\Gamma}{dE}(E) \cdot R(E; qU) dE, \quad (2.8)$$

with A as the normalization of the signal. The expected count rate is then given by

$$\Gamma(qU) = I(qU) + B, \quad (2.9)$$

where B is a constant background rate to account for the measured background electrons.

2.3 Systematic Effects

Several systematic effects arise from the theoretical models as well as the technical limitations of the experiment. A brief overview of these effects is given in this section.

Rear Wall

As the RW is hit by electrons and ions, tritiated molecules are formed on its surface. The electrons emitted in the beta decay of these molecules produce an additional integral spectrum to the one from the tritium molecules in the source [60]. Consequently, this additional spectrum has to be accounted for in the analysis. Due to its small contribution, this effect is neglected in the first two measurement campaigns.

Column Density

Since the column density influences the expected probability of scattering in the source (see Equation 2.6) and therefore the response function (see Equation 2.7), the uncertainty from the limited knowledge of the column density has to be taken into account.

Energy Loss Function

The parameters in the parametrization of the energy loss function (see Equation 2.2.2) are determined from a fit to data from dedicated measurements with a corresponding uncertainty [48]. These uncertainties have to be considered, since the energy loss function is used to determine the response function (see Equation 2.7).

Electron Starting Potential

The plasma in the source defines the starting potential of the electrons [55]. Longitudinal inhomogeneities of the plasma potential cause a shape distortion of the tritium beta spectrum. Since the probability for electrons to undergo inelastic scattering depends on the starting position z in the source, such an inhomogeneity also means that on average scattered electrons have a different starting potential than unscattered electrons [61]. This effect will be referred to as the “plasma” uncertainty.

Magnetic Fields

The source magnetic field B_{src} and pinch magnetic field B_{max} directly influence the transmission function (see Equation 2.2.2) and implicitly the scattering probabilities and therefore the response function. The magnetic field in the analyzing plane B_{ana} also directly impacts the transmission function [54]. Thus, the uncertainty on the values of these fields has to be considered.

Background Overdispersion

Apart from the expected Poissonian distributed background, the distribution can contain an additional component adding to the overall background rate that is not described by a Poissonian distribution [55], referred to as the “non-Poisson” background. This background contribution is eliminated by the SAP setting described in 2.1.4.

Background Energy Slope

The background rate depends on the retarding potential qU , referred to as “qU slope”. Even though this dependency is rather weak, it is important to consider this effect at the endpoint of the spectrum, where the count rate is low. This slope is determined from dedicated measurements [62].

Penning Induced Slope

Stored electrons in the Penning trap between the two spectrometers contribute to the background rate via the creation of positive ions. This background increases until the Penning wipers empty the trap every time the retarding potential is changed [56, 54]. This additional background is referred to as the “Penning slope”. As mentioned in 2.1.4, the PS is not operated anymore since the end of the fourth measurement campaign, eliminating this effect.

Other Systematic Effects

Theoretical calculations of the FSD do not come with an uncertainty. While estimations for this uncertainty can be made, the contribution is small [63]. It is also not implemented in Netrium (see 3.1.2) and therefore not further discussed in this thesis.

Systematic effects arising from the retarding potential dependence of the detector efficiency are corrected, but they have a negligible impact on the neutrino mass and are therefore not considered [64].

Fluctuations of the source activity are estimated to be small and thus neglected.

Chapter 3

Analysis Strategy

3.1 Software

3.1.1 Fitrium

Fitrium is an analysis tool developed for the KATRIN experiment. It is written in C++ and includes a model of the tritium beta spectrum and the experimental setup as well as applications for Monte Carlo data generation and data fitting. When fitting data, the model evaluation and subsequently the integration over the spectrum has to be repeated many times. For a detailed description of Fitrium see [65].

3.1.2 Netrium

Due to many root searches and integrations in the evaluation of the model, the analysis with Fitrium requires a lot of computational power and time. Furthermore, the SAP setting requires 14 model evaluations instead of one and the combination of measurement campaigns as well as the inclusion of systematic uncertainties additionally scale up the computational power and time required.

Because of this, a new analysis tool called Netrium has been developed, mainly in Python. It uses a neural network to approximate the integral spectrum for a given set of input parameters. Netrium has one input node for each parameter and one output node for each retarding energy point in the spectrum. Between the input and output nodes are two hidden layers with 128 nodes each. The structure of the neural network is sketched in Figure 3.1.

For the training of Netrium a set of input parameters, that are sampled according to uniform and normal distributions with different standard deviations, is provided. From these input parameters several million integral spectra are calculated, which then serve as the training data. During the training, the weights are optimized by minimizing the loss function

$$\text{loss}(\mathbf{w}) = \left\langle \left(\frac{R_i^{\text{true}} - R_i^{\text{pred}}(\mathbf{w})}{\langle R_i^{\text{true}} \rangle} \right)^2 \right\rangle, \quad (3.1)$$

where \mathbf{w} are the weights, R_i^{true} the true rates of each sample and $R_i^{\text{pred}}(\mathbf{w})$ are the rates predicted by Netrium. To better enable Netrium to learn the changes to the spectrum, the difference in true and predicted rates is normalized to the sample mean of the true rates.

Since Netrium is used as a method to predict the spectrum for a set of given input parameters, it does not “fit” data in the conventional way. For simplicity however, the prediction of the spectrum will be referred to as a fit hereafter.

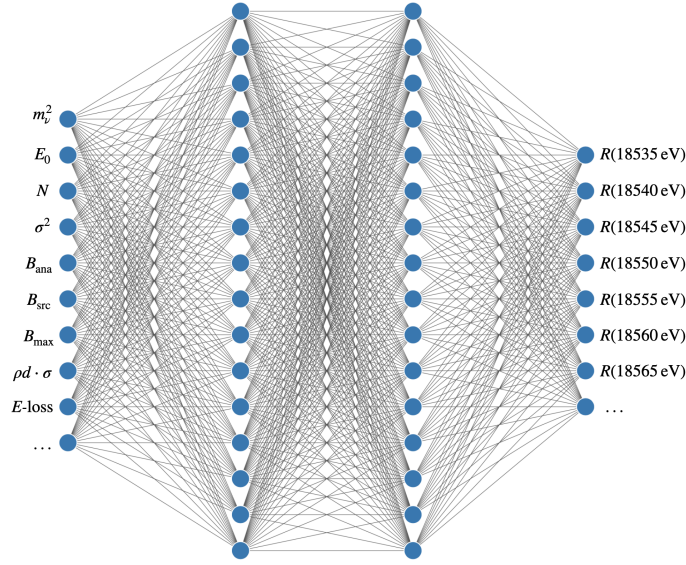


Figure 3.1: Sketched structure of Netrium. There is one input node for each parameter and one output node for each retarding energy point in the spectrum. In between are two hidden layers with 128 nodes each. Figure adapted from [54].

For a detailed description of Netrium as well as a look at the performance, see Chapter 7 of [54].

3.2 Statistical Methods

The most important methods of statistical data analysis used in the light sterile neutrino analysis of data from the KATRIN experiment are briefly explained in this section.

3.2.1 Maximum Likelihood Analysis

The method of maximum likelihood is a technique to infer parameter values from a given set of n measurements of a random variable x that is distributed according to some known probability density function (p.d.f.) $f(x; \boldsymbol{\theta})$ with parameters $\boldsymbol{\theta} = (\theta_1, \dots, \theta_m)$, of which at least one is unknown. The likelihood function

$$\mathcal{L}(\boldsymbol{\theta}) = \prod_{i=1}^n f(x_i; \boldsymbol{\theta}) \quad (3.2)$$

is maximized by the parameters $\hat{\boldsymbol{\theta}}$ that best describe the measured data [66]. Since it is more numerically stable to work with a sum instead of a product, and since most optimization algorithms are design for minimization, instead of maximizing the likelihood function \mathcal{L} , the “neg-log-likelihood” function $-\log(\mathcal{L})$ is minimized [54]. If the p.d.f. $f(x; \boldsymbol{\theta})$ is a normal distribution, the minimization of $-\log(\mathcal{L})$ is equivalent to a χ^2 minimization [66], with

$$-2 \log(\mathcal{L}) = \chi^2. \quad (3.3)$$

In the case of the KATRIN experiment, the measured random variable is the number of counts, $x = N$ and the parameters of interest are the squared neutrino mass m_ν^2 , the endpoint E_0 , the normalization of the signal A and the background rate B : $\boldsymbol{\theta} = (m_\nu^2, E_0, A, B)$. The model prediction μ_i is given by the expected count rate Γ derived in 2.2.3 and the measurement time t_i spent at the retarding energy qU_i :

$$\mu_i = \Gamma(qU_i) \cdot t_i. \quad (3.4)$$

The probability to measure N_i counts at a retarding energy qU_i given a model prediction $\mu_i(\boldsymbol{\theta})$ is described by a Poisson distribution,

$$f(N_i; \mu_i) = \frac{\mu_i^{N_i} \cdot \exp(-\mu_i)}{N_i!}. \quad (3.5)$$

For a large number of counts N_i , the Poisson distribution approaches a normal distribution and a χ^2 minimization according to Equation 3.3 can be used. Finally, the neg-log-likelihood function to infer the parameters $\boldsymbol{\theta}$ from the measured counts \mathbf{N} at retarding energies \mathbf{qU} with measurement times \mathbf{t} is given by [54]

$$-\log(\mathcal{L}(\boldsymbol{\theta}; \mathbf{N}, \mathbf{qU}, \mathbf{t})) = -\sum_{i=1} \log(f(N_i; \mu_i(\boldsymbol{\theta}; qU_i, t_i))). \quad (3.6)$$

The value for $-2\log(\mathcal{L})$ obtained from a fit can be used as a goodness-of-fit test. This will be referred to as the χ^2 -value in the following, even when the fit is done with the method of maximum likelihood, not a χ^2 minimization.

To account for the systematic uncertainties described in 2.3, Netrium uses nuisance parameters. These are included in the minimization of $-\log(\mathcal{L})$ as additional parameters $\boldsymbol{\theta}_{\text{sys}}$. To include the prior knowledge on these parameters, they are constrained by multiplying a pull-term to the likelihood function. In the simplest case, this pull-term is a normal distribution with the best estimate μ_{sys} as the mean and the uncertainty σ_{sys} as the standard deviation [54].

3.2.2 Grid Scan

To infer constraints on the light sterile neutrino parameters, a grid scan is performed over the two-dimensional, logarithmic parameter space spanned by the active-to-sterile neutrino mixing $|U_{e4}|^2$ and the square of the light sterile neutrino mass m_4^2 of size $i \times j$. The index i corresponds to the values for $|U_{e4}|^2$ and the index j to the values for m_4^2 . Each point in the grid is fitted with the corresponding sterile parameters fixed and the standard fit parameters from the neutrino mass analysis, $\boldsymbol{\theta} = (E_0, A, B)$, with the squared neutrino mass set to zero, $m_\nu^2 = 0$. For the null hypothesis as well as each fit in the grid a χ_{ij}^2 is obtained and one can then find the best fit by determining $\chi_{\text{BF}}^2 = \min(\chi_{ij}^2)$. The difference $\Delta\chi_{ij}^2 = \chi_{ij}^2 - \chi_{\text{BF}}^2$ is used to draw the contour at $\Delta\chi_{ij}^2 = \Delta\chi_{\text{crit}}^2$, where $\Delta\chi_{\text{crit}}^2 = 2.30$ at 68.3% C.L. and $\Delta\chi_{\text{crit}}^2 = 5.99$ at 95% C.L. for two degrees of freedom [66]. The applicability of Wilk's theorem [67] has been shown in [68].

3.2.3 Raster Scan

The several systematic effects in the KATRIN experiment, as discussed in 2.3, need to be included when studying the sensitivity of the experiment. In Netrium, the systematic effects are included as nuisance parameters. Each grid scan is done by including one systematic uncertainty in addition to the statistical uncertainty, except for the inclusion of all systematic effects. To investigate the impact of the individual systematic uncertainties for every data set, a raster scan is performed on the grid scan data. Given a set of χ_{ij}^2 values for every point in the $|U_{e4}|^2 \times m_4^2$ grid, the 1σ uncertainty on $|U_{e4}|^2$ is determined for a fixed value of m_4^2 by finding $\Delta\chi_i^2 = \Delta\chi_{\text{crit}}^2$. For one degree of freedom, the 1σ uncertainty is given with $\Delta\chi^2 = 1$ [66]. This value corresponds to $\sigma_{|U_{e4}|^2}^{\text{stat+sys}}$ and the contribution from only the systematic uncertainty is then given by

$$\sigma_{|U_{e4}|^2}^{\text{sys}} = \sqrt{\left(\sigma_{|U_{e4}|^2}^{\text{stat+sys}}\right)^2 - \left(\sigma_{|U_{e4}|^2}^{\text{stat}}\right)^2}. \quad (3.7)$$

This is then repeated for every value of m_4^2 .

3.3 Data Combination

Real data measured by the KATRIN experiment is split up into measurement campaigns, which are in turn split up into many individual runs. Furthermore, each of these runs is measured with a multi-pixel detector and therefore the individual data sets have to be combined, which is briefly discussed in this section.

3.3.1 Combination of Pixels

As described in 2.1.5, the FPD has 148 pixels arranged in a dartboard pattern. Each of these pixels measures an independent spectrum and subsequently every pixel has an individual neg-log-likelihood function. To reduce the amount of model evaluations, several pixels are combined into patches by adding up the counts and averaging the measurement times [54]. For measurement campaigns in the normal analyzing plane setting, all pixels are combined into one uniform patch, while for campaigns in the SAP setting, the pixels are combined into 14 patches, as shown for the case of the KNM-3a measurement campaign in Figure 3.2.

3.3.2 Combination of Runs

The spectrum is measured multiple times during a measurement campaign, resulting in many individual runs. All individual spectra from these runs are combined into one spectrum by adding up the counts as well as the measurement times and averaging the model parameters [54].

3.3.3 Combination of Measurement Campaigns

Parameters that are stable during one measurement campaign, e.g. the column density, are not necessarily equal for different measurement campaigns and averaging of the parameters is not possible. Therefore, the individual neg-log-likelihood functions of all measurement campaigns are combined [54].

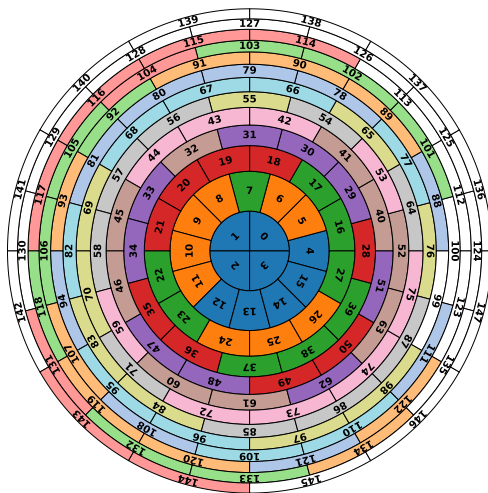


Figure 3.2: The 14 patches used in the analysis of measurement campaigns in the SAP setting, in this case KNM-3a. All pixels that have the same color belong to the same patch.

Chapter 4

Netrium for the Light Sterile Neutrino Analysis

As described in 3.1.2, Netrium vastly improves the computing time when analyzing data from the tritium beta spectrum measurements of the KATRIN experiment and allows the combination of multiple measurement campaigns. It is already successfully used in the neutrino mass analysis [54] and for the reasons stated above the application in the light sterile neutrino analysis would be beneficial. With the two additional sterile neutrino parameters $|U_{e4}|^2$ and m_4^2 and the therefore extended parameter space, the applicability of Netrium has to be validated. The well established software Fitrium (see 3.1.1) is used as a benchmark to compare the following results with Netrium:

1. Light sterile neutrino signal: can Netrium accurately predict the signature of a light sterile neutrino in the spectrum?
2. Individual fits of the beta spectrum for different sterile parameters.
3. Sensitivity contours in the light sterile neutrino parameter space.

4.1 Light Sterile Neutrino Signal

The signature of a light sterile neutrino in the $(3+1)\nu$ framework in the data of the KATRIN experiment is discussed in 1.4.1 and illustrated in Figure 1.3. To show that Netrium properly learns the sterile parameters and subsequently models this signature accurately, two Monte-Carlo copy data sets without statistical fluctuations, called Asimov data sets, are generated with Fitrium. Both are generated based on the KNM-2 measurement campaign: one without a light sterile neutrino, called the null hypothesis, and one with a light sterile neutrino with $|U_{e4}|^2 = 0.01$ and $m_4^2 = (10\text{ eV})^2$. The two parameters for the light sterile neutrino are chosen such that the signature is clearly visible.

The effect of a light sterile neutrino on the spectrum is best visualized by taking the ratio of the $(3+1)\nu$ to the 3ν model, where the signature then shows as a characteristic “dip”-like structure in the ratio of the two spectral data sets. Both spectra can then be fitted with Fitrium and with Netrium, and the ratio of the $(3+1)\nu$ model fit to the 3ν model fit can be taken. This is shown in the top of Figure 4.1. Note that the sterile parameters are not free fit parameters here, but set to the same value as in the Asimov data. The ratio of the Fitrium fits as well as the ratio of the Netrium fits both match the ratio of the data sets very accurately.

To further compare the Netrium and Fitrium results, the ratio of the signature from Netrium and the signature from Fitrium, i.e. the ratio of the two ratios explained above, can be taken. This is shown in the bottom of Figure 4.1. The comparison shows that their ratio deviates by less than $2 \cdot 10^{-4}$ from unity.

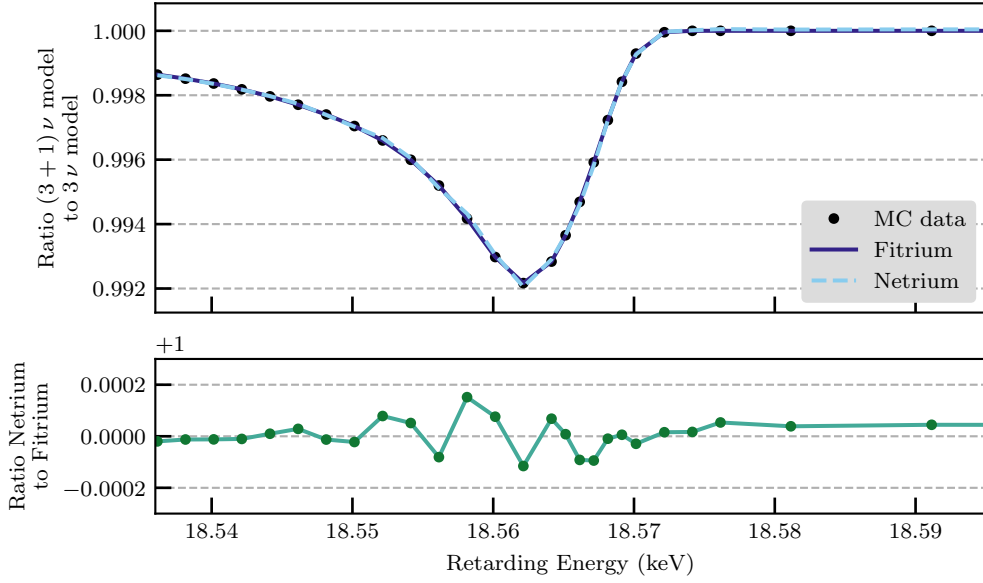


Figure 4.1: Comparison of the light sterile neutrino signature in Neutrino and Fitrium on Asimov data with a light sterile neutrino signal ($|U_{e4}|^2 = 0.01$ and $m_4^2 = (10\text{eV})^2$), and without a light sterile neutrino signal. **Top:** Ratio of the $(3 + 1)\nu$ to the 3ν model for the data sets (black dots), the Fitrium fits (solid dark blue line) and the Neutrino fits (dashed light blue line). **Bottom:** Ratio of the light sterile neutrino signature from Neutrino to the signature from Fitrium, showing an excellent agreement between the two tools.

These results show that Neutrino properly learns the light sterile neutrino parameters and predicts the signature in the spectrum accurately, also in very good agreement with Fitrium.

4.2 Individual Fits

To further show that Neutrino can accurately predict the beta spectrum measured by the KATRIN experiment, the resulting fit and especially the deviance from the actual data can be investigated and compared to that of the Fitrium fit. This is done for the null hypothesis and a fit with sterile parameters, as it is done in a grid scan. The data used is again Asimov data generated with Fitrium and based on the KNM-2 measurement campaign. Note that here the sterile parameters are varied in the fit but the data is generated according to the null hypothesis, i.e. it contains no sterile neutrino signal.

The Fitrium fit of the null hypothesis as well as the residuals from the data normalized to the 1σ statistical uncertainty for both the Fitrium fit and the Neutrino fit is shown in Figure 4.2. The normalized residuals of both fits are below $5 \cdot 10^{-3}\sigma$ and thus in very good agreement with the data. This is of course expected, as the parameters in the fit are the same as in the Asimov data.

The same but with sterile parameters from one point in the grid of a grid scan where the light sterile neutrino would have a huge impact, at $|U_{e4}|^2 = 0.1192$ and $m_4^2 = (9.8715\text{eV})^2$, is shown in Figure 4.3. As expected, the fit deviates largely from the data since the sterile parameters do not match the ones from the Asimov data. The magnitude and the structure of these residuals are very similar for both Fitrium and Neutrino.

Both these fits show that Neutrino can accurately predict the spectrum for the null hypothesis and that the normalized residuals are very similar to those of Fitrium.

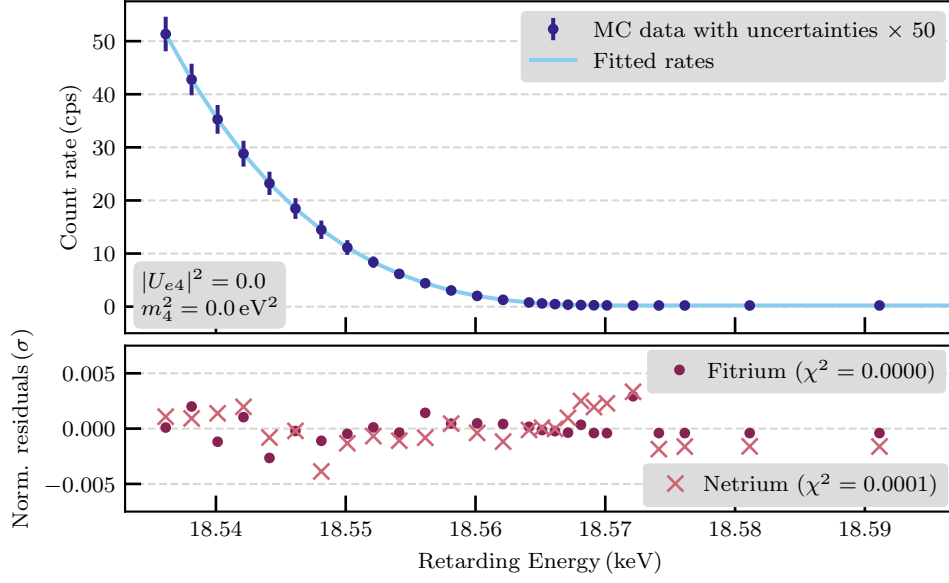


Figure 4.2: Fitrium and Netrium fit of the null hypothesis. **Top:** The data points in dark blue with the 1σ statistical uncertainties (multiplied by 50 for better visibility) and Fitrium fit in light blue. The Netrium fit is not shown, as it shows no visible deviation from the Fitrium fit. **Bottom:** Residuals of the Fitrium and Netrium fit normalized to the 1σ statistical uncertainty.

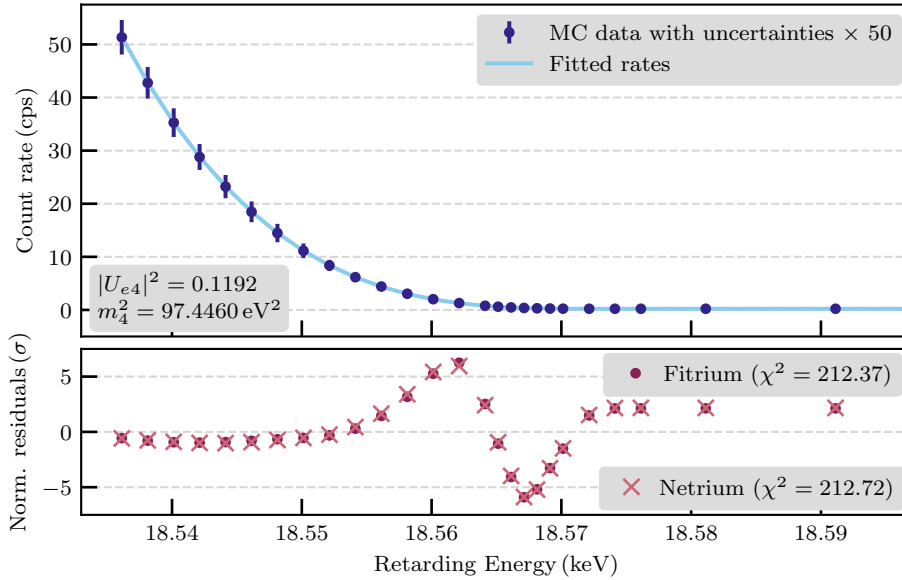


Figure 4.3: Fitrium and Netrium fit with sterile parameters set to $|U_{e4}|^2 = 0.1192$ and $m_4^2 = (9.8715 \text{ eV})^2$. Note that here the sterile parameters are varied in the fit but the data is generated according to the null hypothesis. **Top:** The data points in dark blue with the 1σ statistical uncertainties (multiplied by 50 for better visibility) and Fitrium fit in light blue. The Netrium fit is not shown, as it shows no visible deviation from the Fitrium fit. **Bottom:** Residuals of the Fitrium Netrium fit normalized to the 1σ statistical uncertainty.

4.3 Sensitivity Contours

The final step in the validation is to compare the sensitivity contours from Netrium to the ones from Fitrium. For this, a grid scan (as described in 3.2.2) only including the statistical uncertainty is done and the sensitivity contours on the parameter space of light sterile neutrinos from both tools are then drawn at 95% C.L. and compared. This is done for one Asimov data set generated with Fitrium, based on a measurement campaign with the normal analyzing plane setting and one based on a measurement campaign with the SAP setting. The comparison is done for both settings, since the patch-wise fit done for the data from SAP campaigns requires one model for each patch and therefore also one neural network per patch. Thus, it has to be shown that Netrium also works in the SAP setting. The intervals of the sterile parameters are $|U_{e4}|^2 \in [0.001, 0.5]$ and $m_4^2 \in [1, 1600] \text{ eV}^2$ with a grid size in $|U_{e4}|^2 \times m_4^2$ of 40×30 for the comparison in the normal setting and 20×20 for the comparison in the SAP setting, because of the rather long computing time of the Fitrium grid scan, especially when 14 model evaluations are needed for data from SAP campaigns.

For the measurement campaign in the normal setting, Asimov data based on KNM-1 is used. The resulting sensitivity contours from both Netrium and Fitrium are shown in Figure 4.4. Both contours agree sufficiently well with each other.

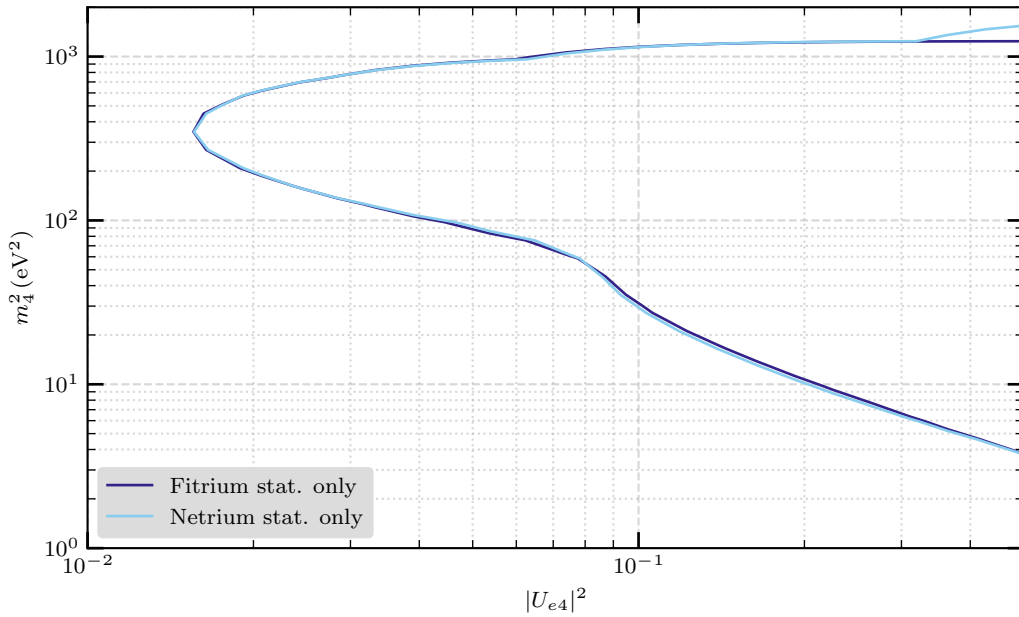


Figure 4.4: Comparison of Netrium and Fitrium sensitivity contours for Asimov data based on KNM-1. The Fitrium and Netrium sensitivity contours are shown in dark blue and light blue, respectively.

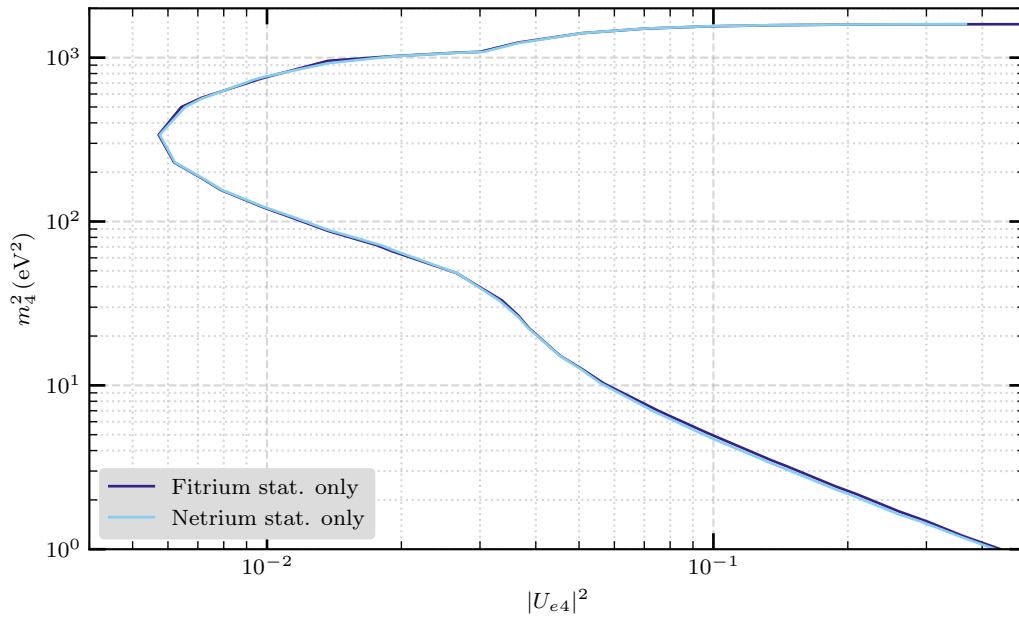


Figure 4.5: Comparison of Netrium and Fitrium sensitivity contours for Asimov data based on KNM-4. The Fitrium and Netrium sensitivity contours are shown in dark blue and light blue, respectively.

The comparison in the SAP setting is done on Asimov data based on KNM-4, and the Netrium and Fitrium sensitivity contours are shown in Figure 4.5. In this case, the contours do also not deviate significantly from each other.

For both the normal and the SAP setting the sensitivity contours obtained from Netrium and Fitrium grid scans agree well with each other, as can be seen in both comparisons.

It has been shown that Netrium can accurately predict the signature of a light sterile neutrino in the spectrum measured by the KATRIN experiment and that the prediction agrees well with the Fitrium fit. Further, the comparison of individual fits for the null hypothesis, as well as with the sterile parameters corresponding to a grid point, of both tools has shown that Netrium performs well in both cases. Lastly, also the sensitivity contours obtained from both tools match fine for both the normal and the SAP setting. From these observations it is concluded that Netrium can be applied in the light sterile neutrino analysis of the KATRIN experiment.

Chapter 5

Pixel Combination for the Light Sterile Neutrino Analysis

To reduce the background in the KATRIN experiment, the SAP setting, as discussed in 2.1.4, was tested as part of the third measurement campaign and is used permanently since the beginning of the fourth measurement campaign. A patch-wise analysis, where multiple pixels of the FPD are combined into one patch, is required for measurement campaigns in this setting, to reduce the impact of the increased spread of the electric potentials and magnetic fields [57]. Since the signal of a light sterile neutrino is located further below the endpoint of the spectrum than the neutrino mass signal, averaging the field values over a larger number of pixels might not have a large impact on the sensitivity. Therefore, less patches could be sufficient for the light sterile neutrino analysis, or patch-wise fitting might not be required at all.

For Fitrium, the tritium beta decay model has to be calculated individually for every patch and for Netrium, every individual model and subsequently every patch requires a separate neural network that has to be trained. Therefore, a reduction of the number of patches would decrease the computation time significantly for both tools, especially when performing a fine binned analysis in the two-dimensional light sterile parameter space. In addition, patch configurations that contain a large number of pixels could enable the usage of the covariance matrix method to include systematic uncertainties in the analysis, as the number of counts per retarding energy is increased, allowing the use of a normal distribution.

To check the impact of an analysis with less patches on the sensitivity and subsequently the necessity of a patch-wise fit, and further to investigate the optimal number of patches, a study on the impact of different patches is performed with Fitrium on three Asimov data sets generated with Fitrium and based on KNM-3a. The first dataset is generated according to the null hypothesis, i.e. with no sterile neutrino signal, while the other two data sets are generated including sterile neutrino signals with two different sterile parameter sets.

5.1 Pixel Combinations

For the study, the pixels of the FPD are grouped in four different ways, as shown for KNM-3a in Figure 5.1:

- 14 patches: The standard patches used for the neutrino mass analysis of SAP campaigns (see Figure 5.1a),
- Four pseudo-patches: Combination of patches $[0, 2]$; $[3, 5]$; $[6, 9]$ and $[10, 13]$ of the standard patches (see Figure 5.1b),

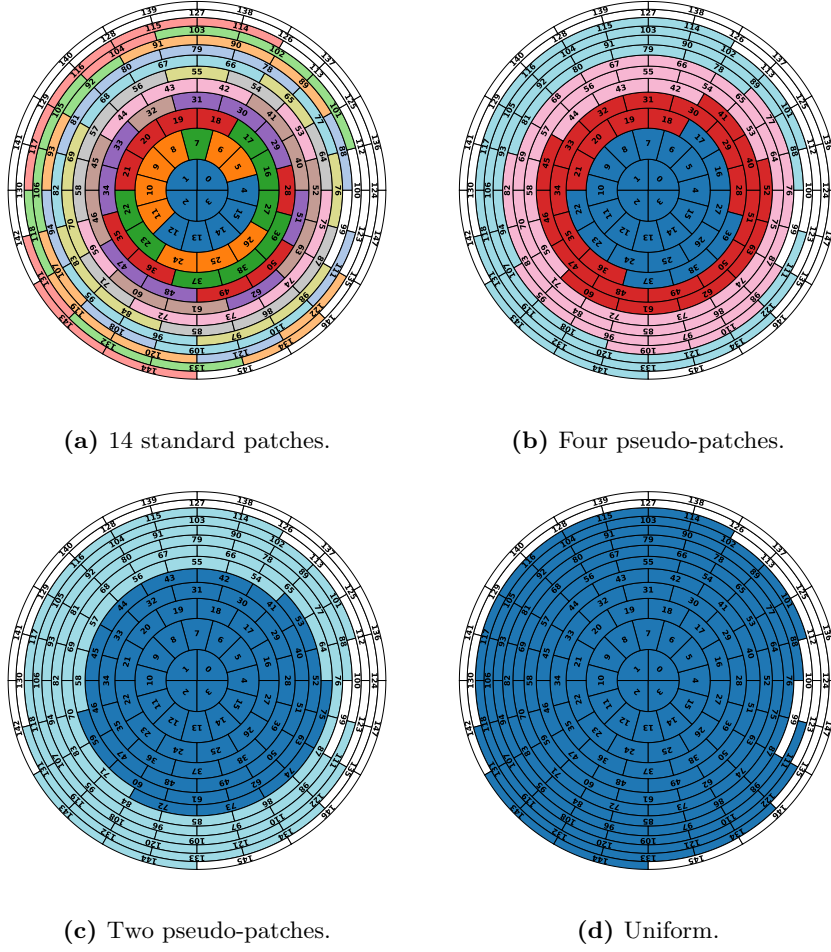


Figure 5.1: The four different pixel combinations used for the study. All pixels that have the same color belong to the same patch. Only the active pixels from KNM-3a are used.

- Two pseudo-patches: Combination of patches [0, 6] and [7, 13] of the standard patches (see Figure 5.1c),
- Uniform: Combination of all patches (see Figure 5.1d).

The systematic effects caused by the rear wall signal and the Penning slope are given individually for each of the 14 standard patches. To account for these in the other configurations, the rear wall signal values are averaged with a weighted mean and the Penning slope is summed up, each for the corresponding patches that are combined.

5.2 Impact of the Pixel Combination for the Null Hypothesis

For the null hypothesis data set, a grid scan (see 3.2.2) is performed with each of the four patches with sterile parameters of $|U_{e4}|^2 \in [0.001, 0.5]$ and $m_4^2 \in [1, 1600] \text{ eV}^2$ on a 20×20 grid, only considering statistical uncertainties. The resulting sensitivity contours at 95% C.L. are shown in Figure 5.2.

Only the uniform sensitivity contour differs visibly from the patch-wise ones. The contours for

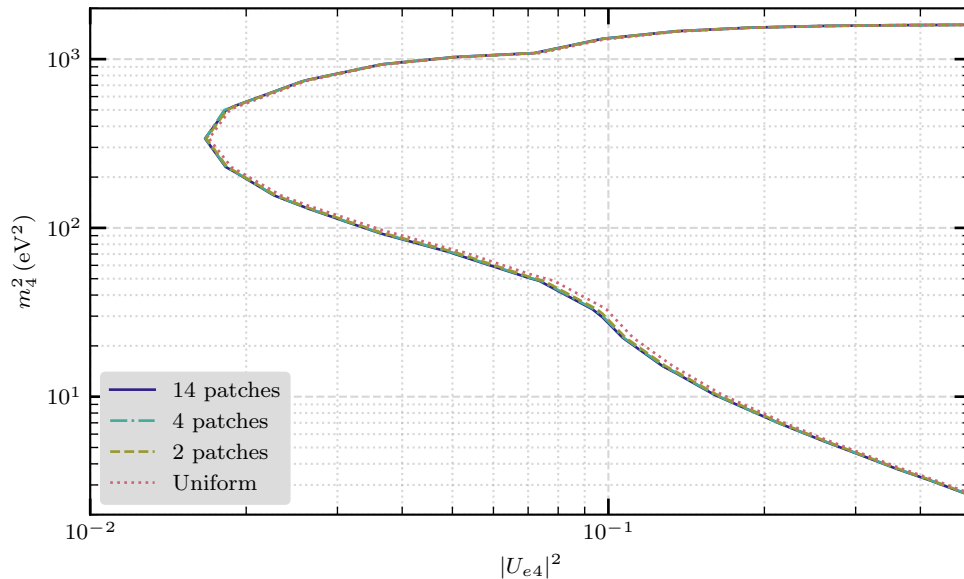


Figure 5.2: Impact of the different patch combinations on the sensitivity contours at 95% C.L. for the null hypothesis.

the two pseudo-patches and four pseudo-patches are hardly distinguishable from the standard case using 14 patches. In the case of the null hypothesis, the two pseudo-patches would therefore already be sufficient

5.3 Impact of the Pixel Combination with a Sterile Neutrino Signal

To investigate the impact of the different patches on data containing a light sterile neutrino signal, two Asimov data sets are generated. For the first data set, the parameters $|U_{e4}|^2 = 0.1$ and $m_4^2 = 30 \text{ eV}^2$ are chosen, since the different sensitivity contours obtained from the null hypothesis grid scan deviate the most at this point in the parameter space (see Figure 5.2). The second data set is generated with sterile parameters of $|U_{e4}|^2 = 0.02$ and $m_4^2 = 200 \text{ eV}^2$, a point in the grid where the sensitivity contours do not deviate very much from each other. With this selection the minimal and maximal impact of the different patch configurations can be estimated. Like for the null hypothesis data set, a grid scan with sterile parameters of $|U_{e4}|^2 \in [0.001, 0.5]$ and $m_4^2 \in [1, 1600] \text{ eV}^2$ on a 20×20 grid with only the statistical uncertainty is performed for both datasets. First, a confidence level of 95% is chosen and then the contours are also drawn at 68.3% C.L., as the lower confidence level allows the examination of how the different patch combinations impact contours that are closed around a potential light sterile neutrino signal.

The sensitivity contours from the grid scan performed on the first data set are shown at 95% C.L. in Figure 5.3 and at 68.3% C.L. in Figure 5.4. At 95% C.L., only the sensitivity contour for all 14 patches and for the four pseudo-patches starts to close around the grid point of the signal. For the same signal at 68.3% C.L., all contours are closed around the grid point of the signal. The uniform contour is further from the signal than the other contours in all of the points, the two-pseudo-patch contour shows only slight deviations from the contour with all 14 patches, while the four-pseudo-patch contour is basically identical with the 14-patch contour.

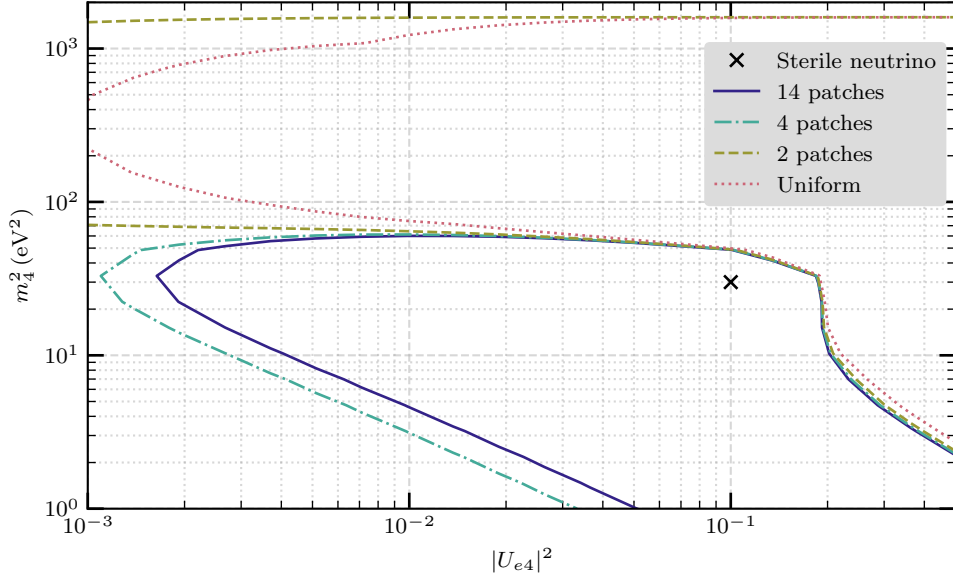


Figure 5.3: Impact of the different patches on the sensitivity contours at 95% C.L. for a simulated sterile neutrino signal with $|U_{e4}|^2 = 0.1$ and $m_4^2 = 30 \text{ eV}^2$. The simulated sterile neutrino signal is marked by the black cross.

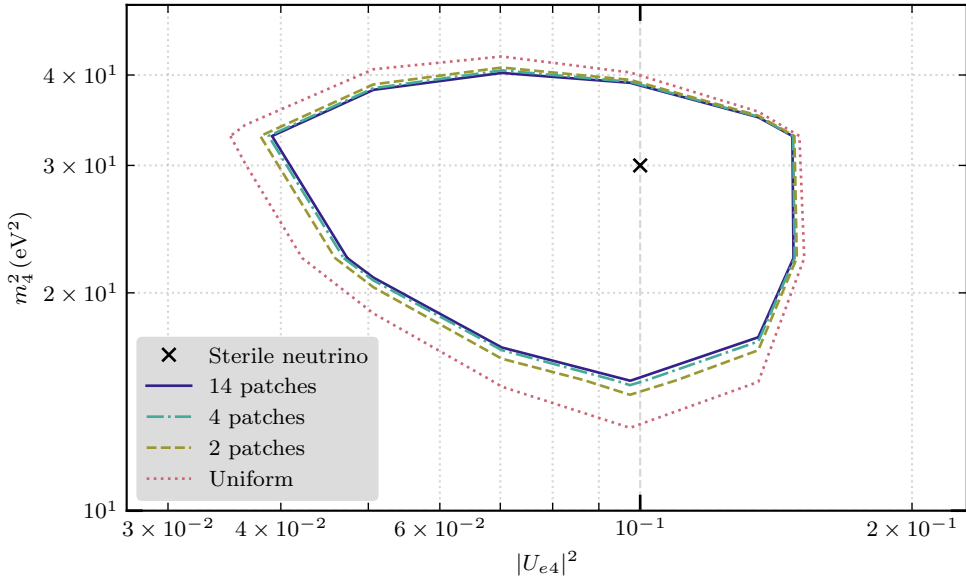


Figure 5.4: Impact of the different patches on the sensitivity contours at 68.3% C.L. for a simulated sterile neutrino signal with $|U_{e4}|^2 = 0.1$ and $m_4^2 = 30 \text{ eV}^2$. The simulated sterile neutrino signal is marked by the black cross.

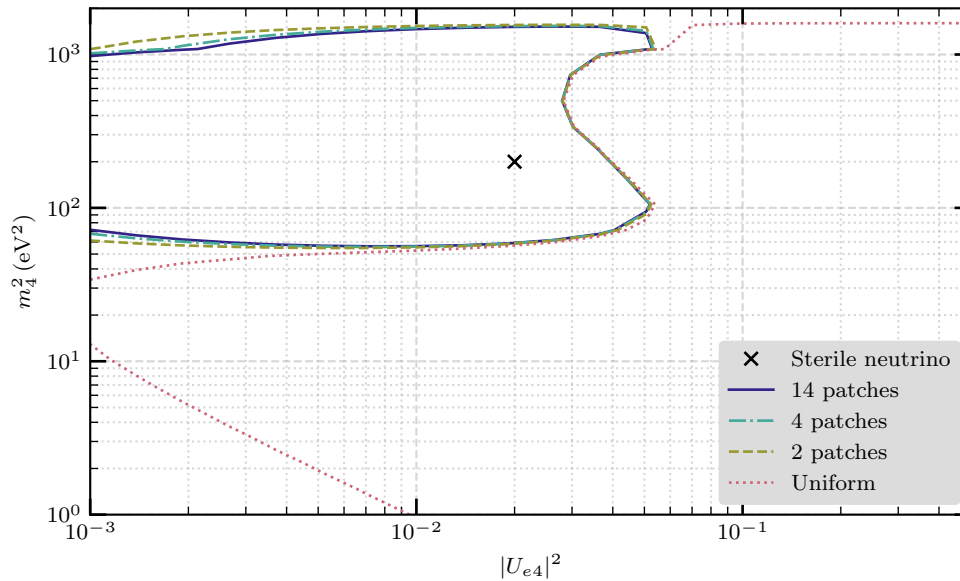


Figure 5.5: Impact of the different patches on the sensitivity contours at 95% C.L. for a simulated sterile neutrino signal with $|U_{e4}|^2 = 0.02$ and $m_4^2 = 200 \text{ eV}^2$. The simulated sterile neutrino signal is marked by the black cross.

The same is done for the second data set with sterile parameters where the sensitivity contours do not deviate very much from each other. Again, this is done for both 95% C.L. and 68.3% C.L., and the resulting sensitivity contours are shown in Figure 5.5 and Figure 5.6, respectively. At 95% C.L., all but the uniform contour start to close around the grid point of the signal. At 68.3% C.L. the contours of all patches are closed around the signal, while they show the same behaviour as for the $(0.1, 30 \text{ eV}^2)$ sterile neutrino signal: the uniform contour is further from the signal than the other contours, the two-pseudo-patch contour shows only slight deviations from the contour with all 14 patches and the four-pseudo-patch contour is basically identical with the 14-patch contour.

From these results it can be concluded that an optimal choice for the patch configuration in the light sterile neutrino analysis of SAP campaigns would be the four pseudo-patches. With this configuration, the parameter space is reduced by a factor of 3.5, while the resulting sensitivity contours are almost identical with the 14-patch contours for all cases except the $(0.1, 30 \text{ eV}^2)$ sterile neutrino signal. For this signal the four-patch contour still starts to close around the signal.

Since the standard systematic contributions are provided for the 14 standard patches, as used in the neutrino mass analysis, a separate calculation would be needed for each new pseudo-patch configuration. Therefore, the standard 14-patch configuration is used in this thesis. For future analyses the patch number could be reduced, given that the pseudo-patch-wise systematic inputs are provided.

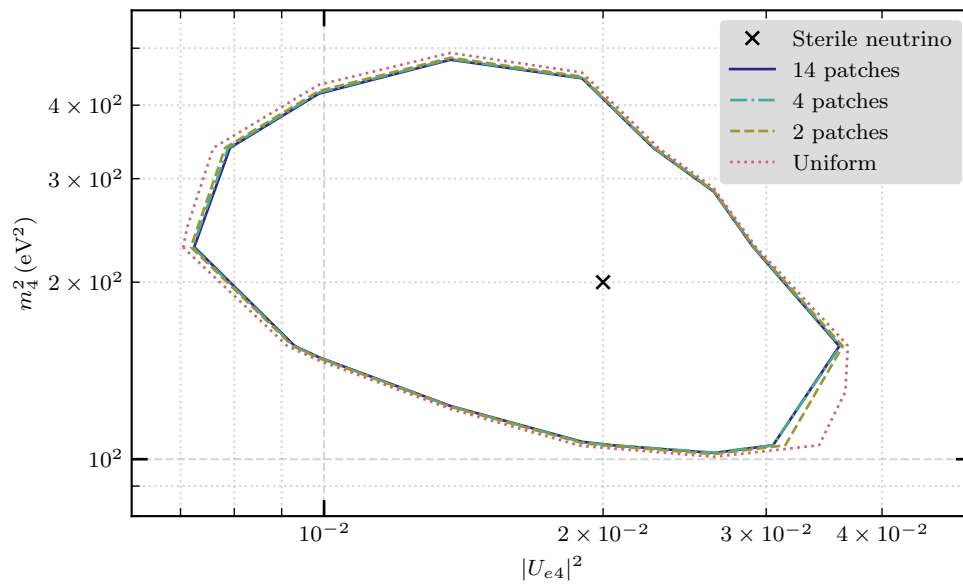


Figure 5.6: Impact of the different patches on the sensitivity contours at 68.3% C.L. for a simulated sterile neutrino signal with $|U_{e4}|^2 = 0.02$ and $m_4^2 = 200 \text{ eV}^2$. The simulated sterile neutrino signal is marked by the black cross.

Chapter 6

Sensitivity of the First Five Measurement Campaigns

The KATRIN experiment is taking data for the neutrino mass analysis since 2019 with five measurement campaigns that have undergone quality control. Data from these measurement campaigns can also be used to search for light sterile neutrinos. In Chapter 4, the applicability of Nefit was validated and it is now used for a sensitivity study of the first five measurement campaigns. Since Nefit enables the combination of multiple measurement campaigns, the combined sensitivity of all campaigns is studied. Furthermore, the impact of systematic uncertainties on the sensitivity is investigated and the combined sensitivity of all measurement campaigns is compared to results from other experiments that are sensitive to light sterile neutrinos. Lastly, the statistics-only sensitivities for different fit ranges are analyzed. The data used for the study are Asimov data sets generated with FitFermi, one for each of the measurement campaigns. As in the neutrino mass analysis, KNM-3a and KNM-3b are considered as separate data sets here.

6.1 Individual and Combined Sensitivity

The sensitivity on the light sterile neutrino parameter space is obtained from a grid scan (see 3.2.2) with sterile parameters of $|U_{e4}|^2 \in [0.001, 0.5]$ and $m_4^2 \in [1, 1600] \text{ eV}^2$ with a grid size of 50×50 . Using Nefit, the analysis can be performed separately for each individual measurement campaign as well as the combination of all campaigns.

First, the grid scans are calculated including only the statistical uncertainty for all individual as well as combined measurement campaigns. The resulting sensitivity contours at 95% C.L. are shown in Figure 6.1. While KNM-1, KNM-3a and KNM-3b are very similar, the sensitivity increases with KNM-2, KNM-4 and KNM-5. Of course, the sensitivity is strongly correlated with the number of electrons measured in the 40 eV fit range, which is shown in Table 6.1. By combining all measurement campaigns, a large increase in sensitivity is gained.

Campaign	KNM-1	KNM-2	KNM-3a	KNM-3b	KNM-4	KNM-5	Combined
Number of electrons in 40 eV fit range (10^6)	2.0	4.3	1.1	1.4	10.2	16.8	35.8
Number of electrons in 60 eV fit range (10^6)	3.5	8.3	2.0	2.8	19.5	35.8	71.9
Number of electrons in 90 eV fit range (10^6)	10.1	33.3	7.7	11.0	213.8	290.4	566.3

Table 6.1: Number of electrons in different fit ranges for all measurement campaigns and the combination of all campaigns.

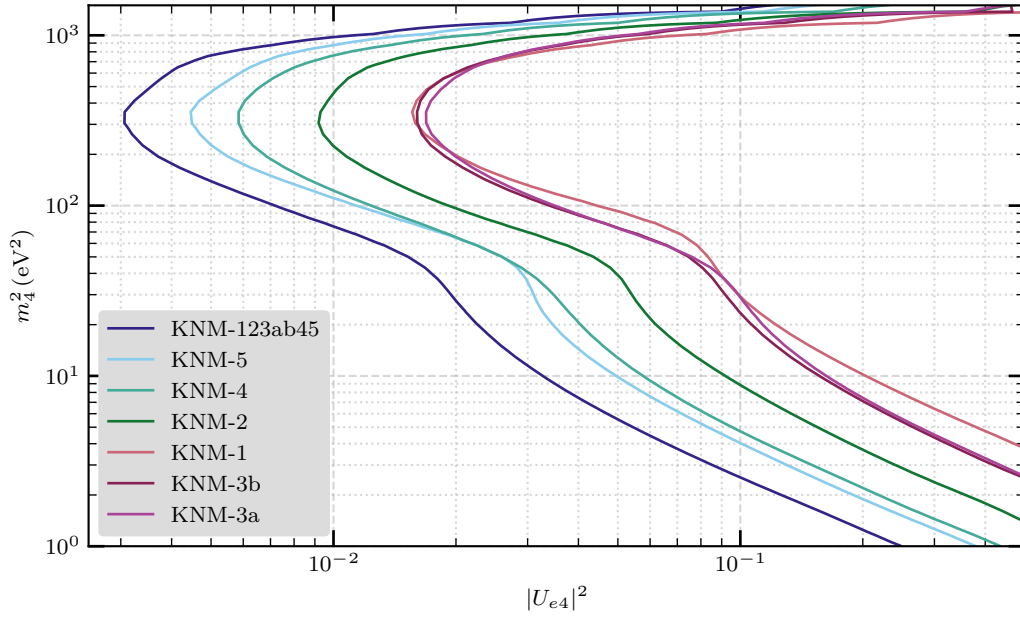


Figure 6.1: Sensitivity contours for all individual measurement campaigns and the combination of all measurement campaigns including only the statistical uncertainty.

For the actual sensitivity, all the uncertainties caused by the various systematic effects have to be included. Again, grid scans are performed on the same Asimov data as above, but now including all systematic uncertainties in all measurement campaigns as well as the combination of all campaigns. This slightly decreases the sensitivity of all individual measurement campaigns and the combination of all campaigns, as shown in Figure 6.2. The impact on the sensitivity contours is rather small, however not negligible.

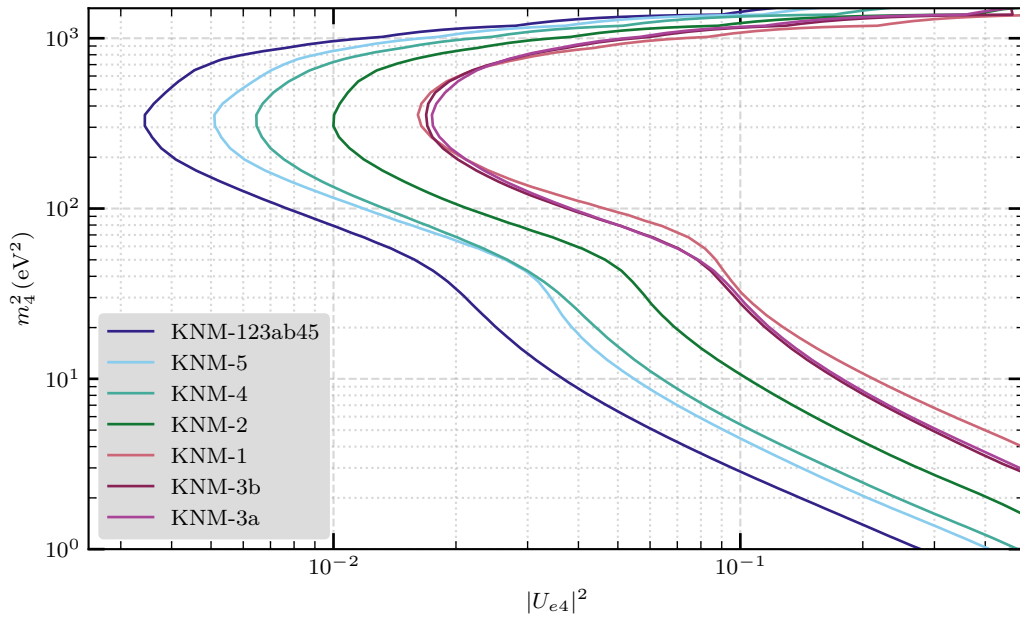


Figure 6.2: Sensitivity contours for all individual measurement campaigns and the combination of all measurement campaigns including all systematic uncertainties.

6.2 Systematic Uncertainties

The sensitivities of individual measurement campaigns including only statistical uncertainties as well as with the addition of all systematic uncertainties have been shown in the preceding section. Now, the impact of every individual systematic uncertainty is investigated. For this, one grid scan is performed for each systematic effect, including the systematic uncertainty of this effect in addition to the statistical uncertainty. Like before, the grid scans (see 3.2.2) are performed with sterile parameters of $|U_{e4}|^2 \in [0.001, 0.5]$ and $m_4^2 \in [1, 1600] \text{ eV}^2$ with a grid size of 50×50 . To investigate the contribution of only the individual systematic effects, a raster scan, as described in 3.2.3, is performed with the fit results obtained from these grid scans. The result shows the 1σ uncertainty on the active-to-sterile mixing $|U_{e4}|^2$ for every sterile mass m_4^2 . Since in the KNM-3b measurement campaign all of the possible systematic effects are present, the results of the raster scan are shown for this measurement campaign in Figure 6.3. Another way to examine the impact of the individual systematic uncertainties is to study the impact on $|U_{e4}|^2$ for individual masses. This is done for values of m_4^2 in the grid which are close to the powers of ten and shown in Figure 6.4.

For comparison, also the results of the raster scan for KNM-5 are shown in Figure 6.5, where the uncertainty from the non-Poissonian background and the Penning slope are eliminated (see 2.3). Furthermore, the systematic uncertainties have more impact in KNM-5, due to the increased statistical precision. Analogous to KNM-3b before, the impact of the systematic uncertainties for individual values of m_4^2 is also shown for KNM-5 in Figure 6.6. The raster scan results as well as the impact for different values of m_4^2 of all other measurement campaigns are shown in Appendix A.

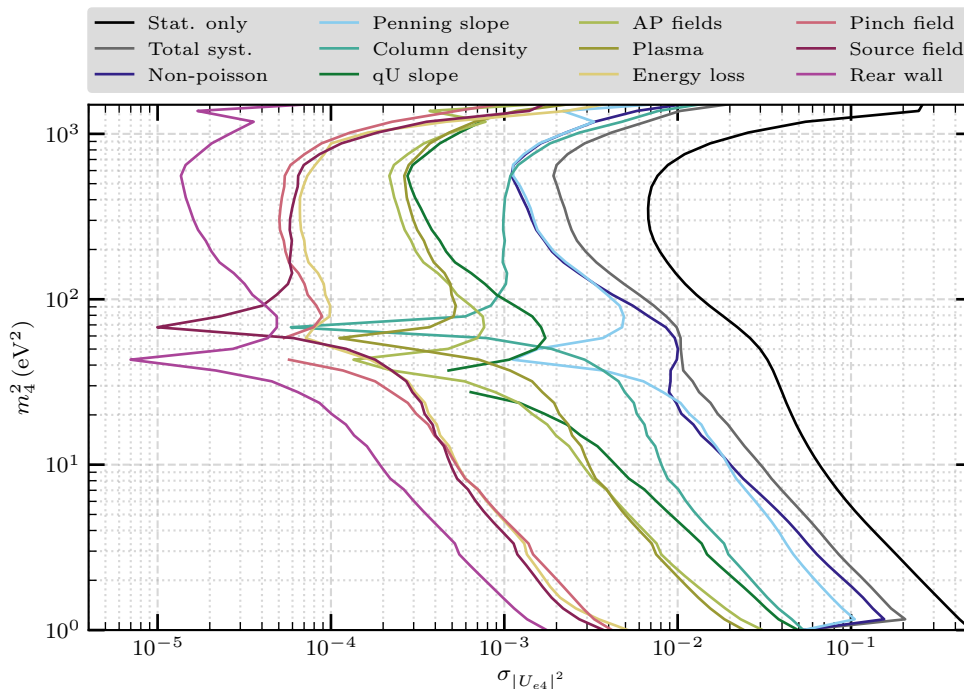


Figure 6.3: Impact of individual systematic uncertainties on $|U_{e4}|^2$ in KNM-3b obtained from a raster scan.

For KNM-3b, the total systematic uncertainty is dominated by the non-Poissonian background and the background from the Penning slope up to about 600 eV^2 . From then on, the column density uncertainty has the largest impact. The impact of the qU slope is rather strong for small masses and decreases for higher masses, since this slope becomes less prominent when the statistics increase deeper into the beta spectrum. The impact of the uncertainty on the magnetic fields in the analyzing plane and the plasma uncertainty are rather similar. Much less impact on the total systematic uncertainty comes from the uncertainties on the energy loss function as well as the pinch and source magnetic fields. Overall, the rear wall uncertainty has the least impact.

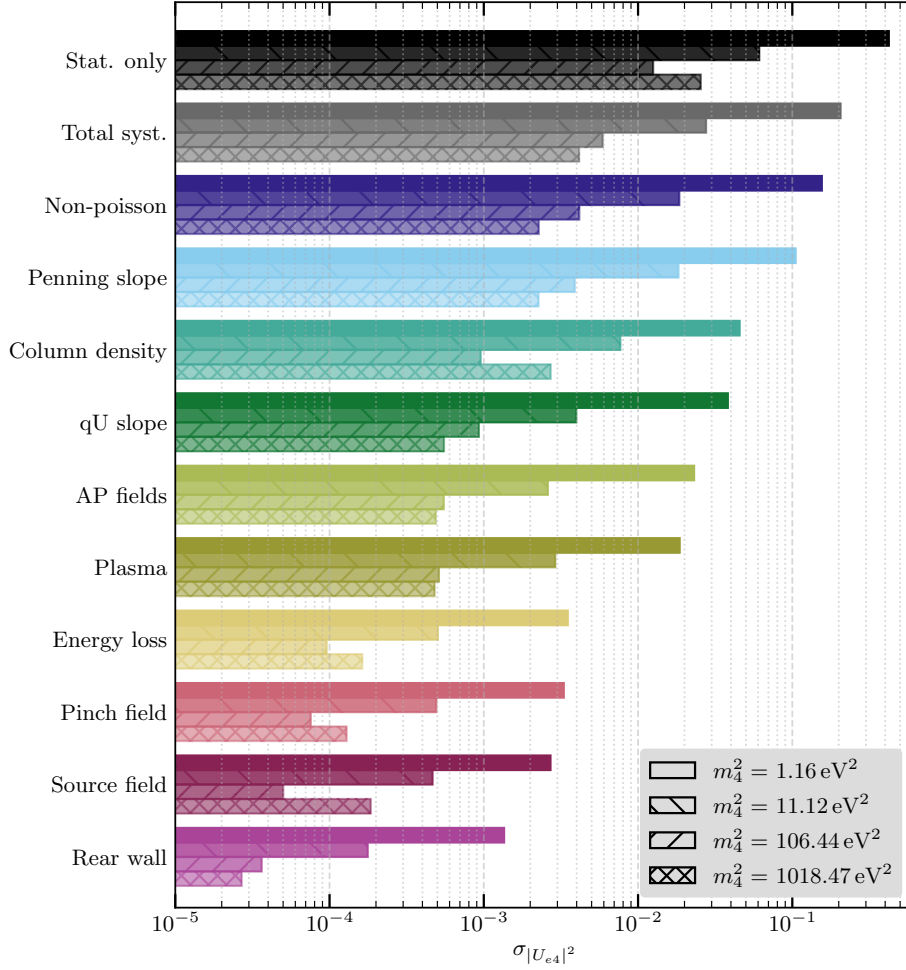


Figure 6.4: Impact of individual systematic uncertainties for different values of m_4^2 in KNM-3b obtained from a raster scan.

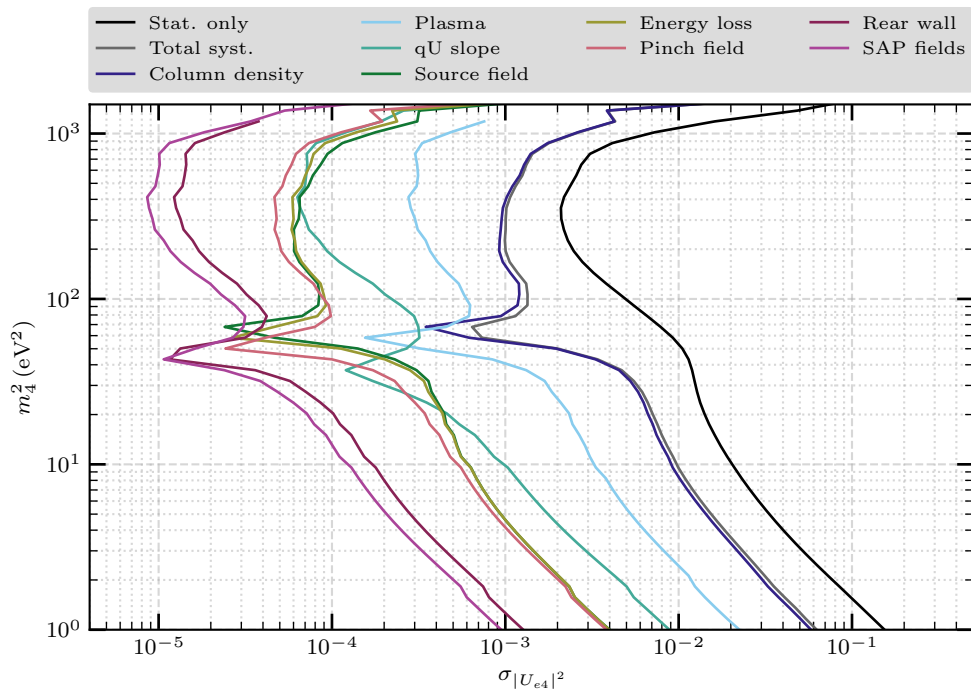


Figure 6.5: Impact of individual systematic uncertainties on $|U_{e4}|^2$ in KNM-5 obtained from a raster scan.

In KNM-5, the two dominant causes for systematic uncertainties, namely the non-Poissonian background and the background from the Penning slope, are eliminated. Thus, the total systematic uncertainty is strongly dominated by the column density uncertainty, followed by the plasma uncertainty. The qU slope shows a similar behaviour as in KNM-3b, although the impact for lower masses is much less, due to the large increase in statistics from KNM-3b to KNM-5. Like for KNM-3b, the impact of the uncertainty on the energy loss function as well as the pinch and source magnetic fields are rather similar. Again, the rear wall uncertainty has a small overall impact but not the lowest, which comes from the uncertainty on the SAP fields, because the measurement precision of these magnetic fields was improved between KNM-3b and KNM-5. Although the magnitude of the systematic uncertainties depends on the light sterile neutrino mass, their general ordering is very similar to the systematic uncertainties on m_ν^2 from the neutrino mass analysis of the corresponding measurement campaigns [69].

Something that is apparent when looking at the results from the raster scans in Figure 6.3 and Figure 6.5 is that in the mass region of about $(30 - 80) \text{eV}^2$, the lines describing the impact on $|U_{e4}|^2$ are drawn towards lower values. This behaviour can also be observed for all other raster scans (see Appendix A). A possible explanation is that the measurement time is very long at this corresponding retarding energy range and the impact of systematic uncertainties is therefore reduced, if they depend on the measurement time. In some cases, e.g. KNM-3b, the contours also have a gap in this mass region, which is the case for masses where the contribution from only the systematic uncertainty (see Equation 3.7) is undefined because the expression in the root becomes negative, i.e. the contribution from the statistical uncertainty is larger than the contribution from the statistical and systematic uncertainty combined. This happens for masses where both contributions are very small and very similar, and it could therefore just be a numerical issue. The exact cause for this behaviour is under investigation.

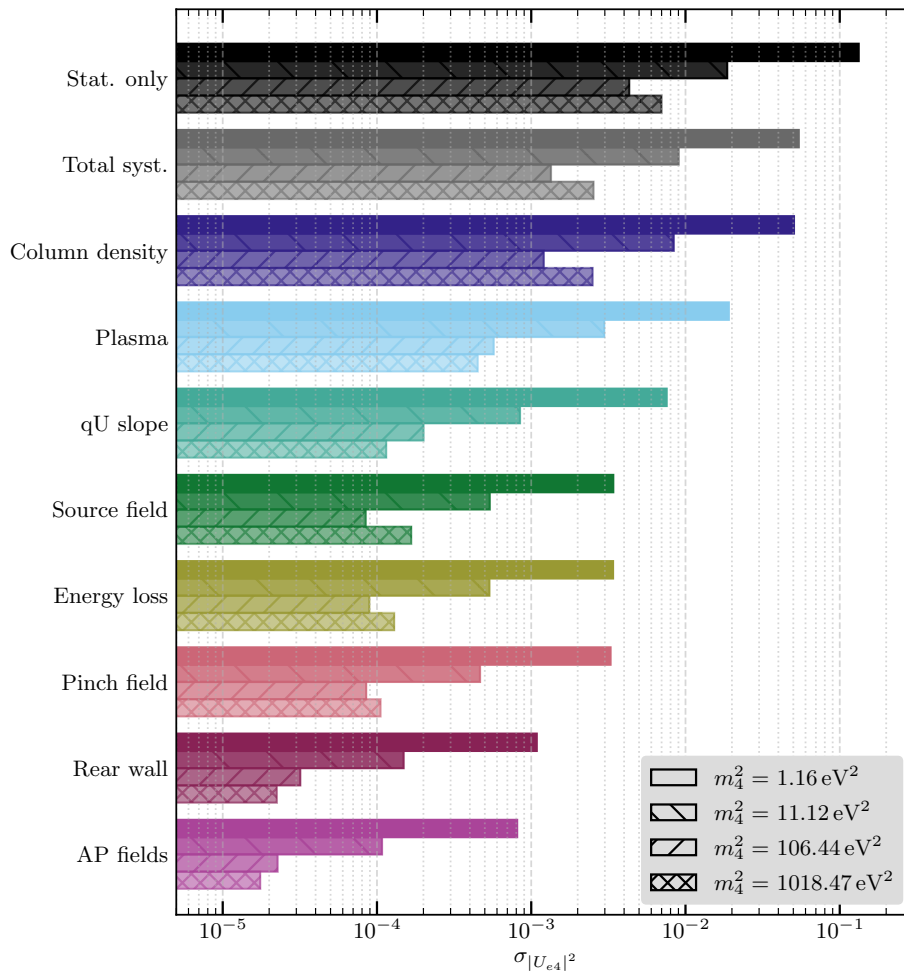


Figure 6.6: Impact of individual systematic uncertainties for different values of m_4^2 in KNM-5 obtained from a raster scan.

6.3 Comparison with Other Experiments

The sensitivity of the first five measurement campaigns of the KATRIN experiment on the light sterile neutrino parameter space obtained with Neutrino can now be compared to the results of short-baseline electron (anti-)neutrino disappearance experiments and especially the parameter space of current anomalies, as discussed in 1.4.2. Thus, a grid scan with sterile parameters of $|U_{e4}|^2 \in [0.001, 0.5]$ and $m_4^2 \in [0.1, 1600] \text{ eV}^2$ and a grid size of 150×150 is done, with the inclusion of all systematic uncertainties. For comparison, the same grid scan is also done only including the statistical uncertainty. In difference to the grid scans performed before, the lower boundary for m_4^2 is extended from 1 eV to 0.1 eV to be able to also include the parameter space up to the maximal value for $|U_{e4}|^2$. Furthermore, the grid size is increased to get a smoother contour. As discussed in 1.4.1, with $\Delta m_{41}^2 \approx m_4^2$ (since $m_4 \gg m_i$) and Equation 1.27, the resulting sensitivity can be compared to short-baseline electron (anti-)neutrino disappearance experiments, which is shown in Figure 6.7.

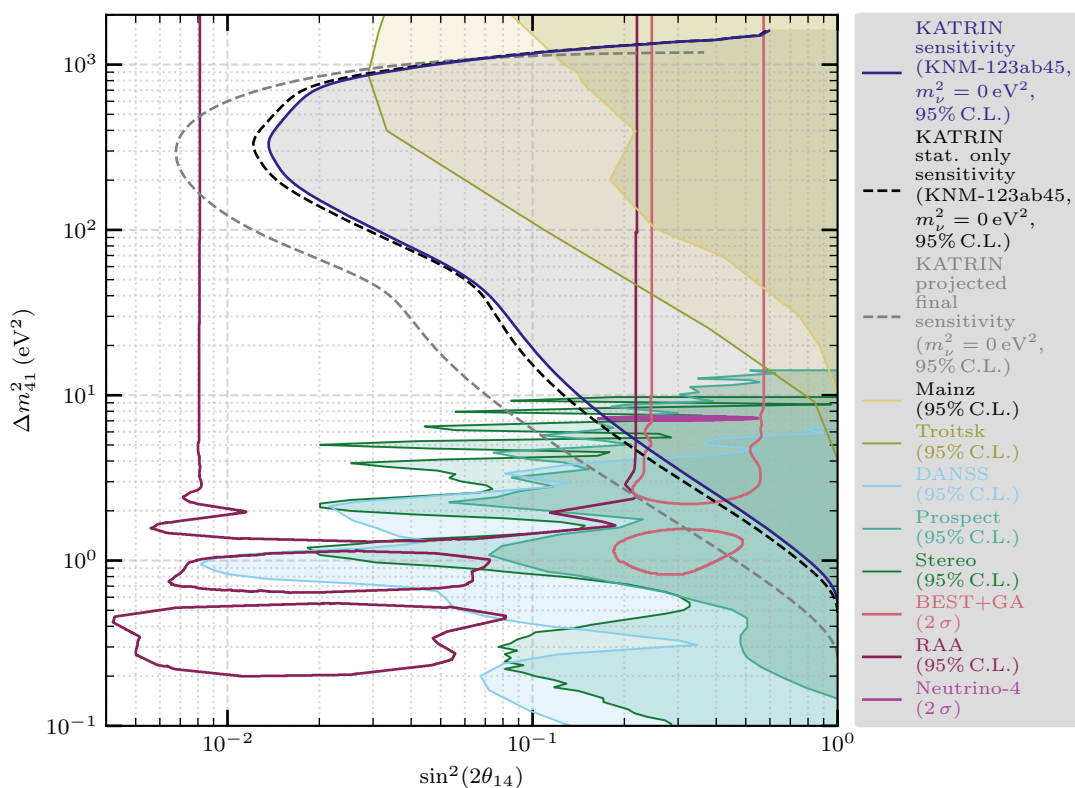


Figure 6.7: The current parameter space of light sterile neutrinos with restrictions from various experiments. For the BEST+GA, RAA and Neutrino-4 experiment the allowed part of the parameter space according to their respective results is shown. For the other experiments, the excluded part of the parameter space not allowed from their results is shown shaded. The parts of the parameter space allowed by the BEST+GA and RAA are in tension as they have no real overlap. The PROSPECT and STEREO experiments exclude the claimed observation of Neutrino-4. Also shown are the Mainz and Troitsk experiments, the predecessors of the KATRIN experiment. The sensitivity of the first five measurement campaigns of the KATRIN experiment only including the statistical uncertainty is shown by the black dashed line and the actual sensitivity with the inclusion of all systematic uncertainties is shown in dark blue. With this sensitivity, a majority of the BEST+GA parameter space could potentially be probed, especially the part currently not excluded by other experiments.

The combined sensitivity shows that with the first five measurement campaigns of the KATRIN experiment a large part of the BEST+GA parameter space as well as the currently unexcluded region, as indicated in Figure 1.4 by the shaded red area, could be probed. Furthermore, almost all of the parameter space from the claimed observation of the Neutrino-4 experiment could potentially be excluded, in addition to the results of the PROSPECT and STEREO experiments.

6.4 Extended Fit Range

For all the studies presented up to now, the same standard fit range as in the neutrino mass analysis of 40 eV below the endpoint was used. An increase of this range could be beneficial for the sensitivity in the light sterile neutrino analysis because of vastly increased statistics due to the amount of electrons measured in a wider fit range, which can be seen in Table 6.1 for the standard 40 eV fit range, as well as two extended fit ranges of 60 eV and 90 eV. This therefore allows to search for an extended set of sterile neutrino masses. The 90 eV fit range is chosen since this is the largest fit range available with the current data from the KATRIN experiment, and the 60 eV range is chosen as a median step between the standard and maximum fit range. To examine the benefits of this extension of the fit range, two additional grid scans in the 60 eV and 90 eV range are performed on all combined data sets, with $m_\nu^2 = 0 \text{ eV}^2$ and only including statistical uncertainties. While the range of the active-to-sterile mixing is $|U_{e4}|^2 \in [0.001, 0.5]$ for the grid scans of all fit ranges, the range of the squared mass is $m_4^2 \in [0.1, 1600] \text{ eV}^2$ for the 40 eV range, $m_4^2 \in [0.1, 3600] \text{ eV}^2$ for the 60 eV range and $m_4^2 \in [0.1, 8100] \text{ eV}^2$ for the 90 eV range. For the extended fit ranges also the grid size in $|U_{e4}|^2 \times m_4^2$ is increased from 50×50 for the standard 40 eV range to 50×100 for the 60 eV range and 50×150 for the 90 eV range, to still obtain smooth contours from a larger grid. The sensitivity contours at 95% C.L. resulting from these three grid scans are shown in Figure 6.8.

As expected, for extended fit ranges the sensitivity contours cover much more of the parameter space in the larger mass region. But also the sensitivity on the active-to-sterile mixing in the lower mass region increases significantly with the extended range, improving the ability to probe the parameter space of the light sterile neutrino anomalies discussed in 1.4.2. Further investigation, regarding the inclusion of systematic uncertainties and the structure of the sensitivity contours at larger masses is required.

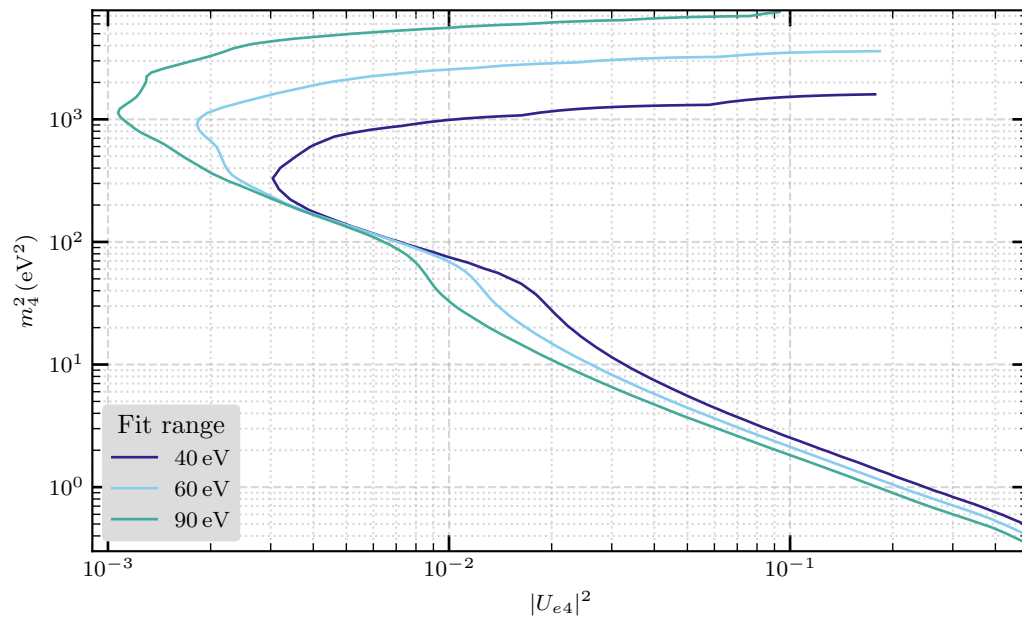


Figure 6.8: Comparison of the sensitivity contours with the normal 40 eV and the extended 60 eV and 90 eV fit range obtained from statistics only grid scans.

Chapter 7

Conclusion

In this thesis, several studies concerning the light sterile neutrino analysis of the KATRIN experiment have been performed. For the standard neutrino mass analysis, the 148 detector pixels are combined into 14 patches and the data is further divided into multiple measurement campaigns. This makes the analysis computationally challenging, since every data set is described by its own model. Therefore, a neural network called Netrium has been developed for the neutrino mass analysis.

Netrium was adapted for the light sterile neutrino analysis with the two additional sterile neutrino parameters $|U_{e4}|^2$ and m_4^2 . Subsequently, this was validated by comparing various results from the well established analysis tool Fitrium to Netrium. First, the signature of a simulated sterile neutrino in the data was fitted with both tools and compared, which showed that Netrium can predict the signature of a light sterile neutrino in the spectrum accurately. Next, individual fits were performed with both tools for different sterile neutrino parameters and compared. The results show that the Netrium fit works well, also in comparison to the Fitrium fits. After that also the sensitivity contours obtained from both Fitrium and Netrium grid scans were compared, which agree well with each other. From these observations it was concluded that Netrium can be applied in the light sterile neutrino analysis.

A lower amount of patches would, among other advantages, significantly decrease the computational effort required in the light sterile neutrino analysis. Therefore, it was investigated how much a decrease of patches affects the statistics-only sensitivity of the KATRIN experiment on the parameter space of light sterile neutrinos. For this, four different patch configurations were considered for a study on Asimov data. To this end, the sensitivity contours for different patches from a grid scan on a data set containing no light sterile neutrino signal are compared. It is found that only the sensitivity contour from a uniform patch differs visibly from the patch-wise ones. The same was repeated for the sensitivity contours from grid scans performed on two data sets that contain a light sterile neutrino signal. The results have shown that in most cases the sensitivity contours from four pseudo-patches are very similar to the ones from the standard case of 14 patches. All in all the four pseudo-patches could be sufficient for the light sterile neutrino analysis, reducing the parameter space by a factor of 3.5. To apply this however, the pseudo-patch-wise systematic inputs would have to be provided, as these were just averaged for this study.

Finally, Netrium is used for a sensitivity study on the data of the first five measurement campaigns. First, the sensitivities of individual measurement campaigns were compared to each other and the combined sensitivity of all campaigns. As expected, a huge increase in sensitivity is gained by combining the data sets. The impact of individual systematic uncertainties was then investigated for all measurement campaigns by doing a raster scan and shown as an example for KNM-3b and KNM-5. The general ordering of the effects is very similar to the systematic uncertainties on m_ν^2 from the neutrino mass analysis of the corresponding measurement campaigns. For a certain

mass region it was observed that the systematic uncertainty on $|U_{e4}|^2$ is drawn towards lower values, which requires further investigation. The sensitivity from the combination of all measurement campaigns was then compared to the current parameter space of light sterile neutrinos, showing that important parts of the light sterile neutrino parameter space could be excluded with the data from the first five measurement campaigns. These include the part of the gallium anomaly currently not excluded by oscillation experiments as well as almost all of the parameter space corresponding to the claimed observation of the Neutrino-4 experiment. Lastly, the statistics-only sensitivity from the standard fit range and two extended fit ranges were compared. As expected, for extended fit ranges the sensitivity contours cover much more of the parameter space in the larger mass region. But also the sensitivity on the active-to-sterile mixing in the lower mass region increases significantly with the extended range. An extended fit range could be used for future analyses.

Appendix A

Systematic Uncertainties of All Measurement Campaigns

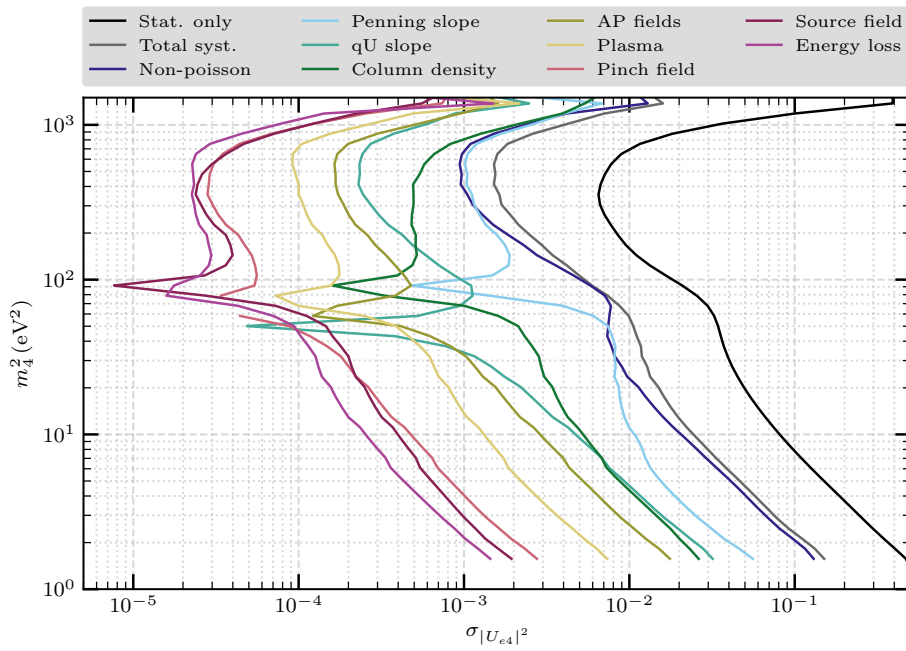


Figure A.1: Impact of individual systematic uncertainties in KNM-1 obtained from a raster scan.

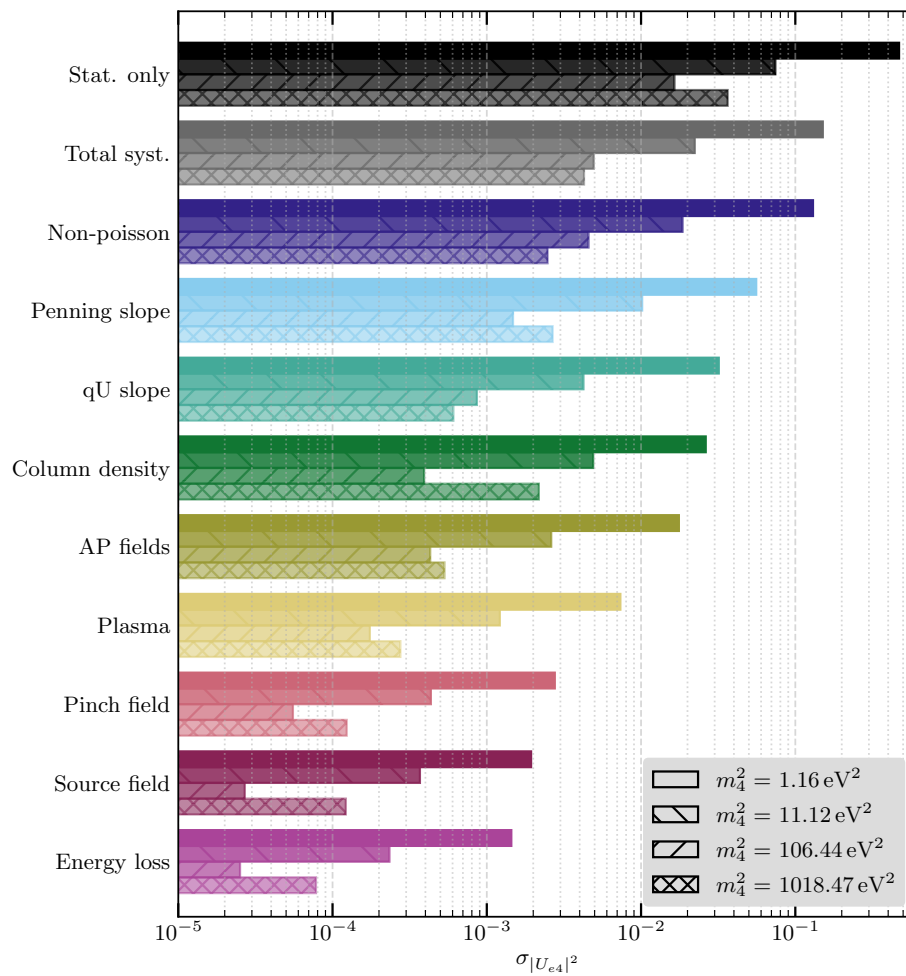


Figure A.2: Impact of individual systematic uncertainties for different values of m_4^2 in KNM-1 obtained from a raster scan.

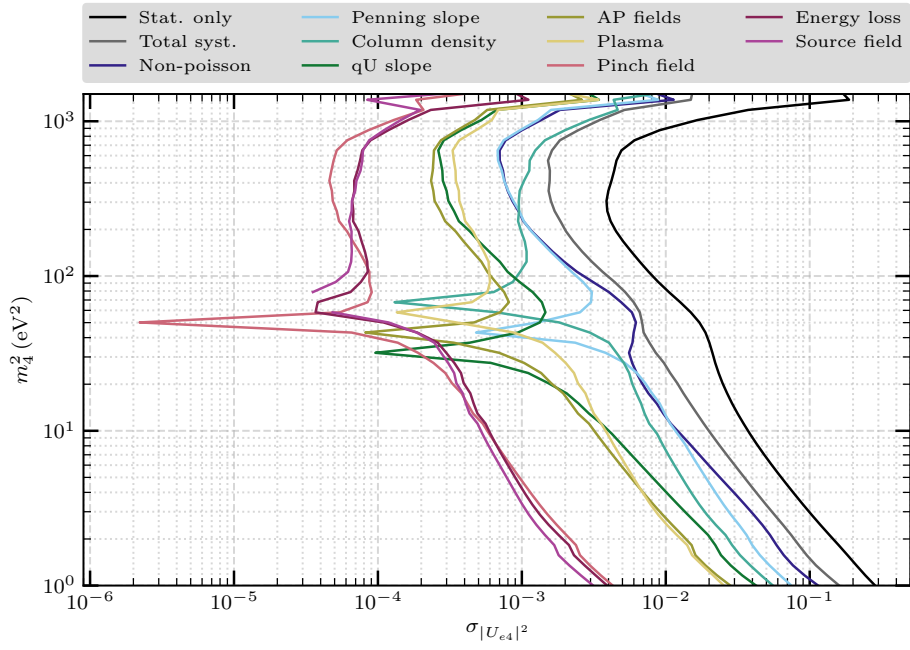


Figure A.3: Impact of individual systematic uncertainties in KNM-2 obtained from a raster scan.

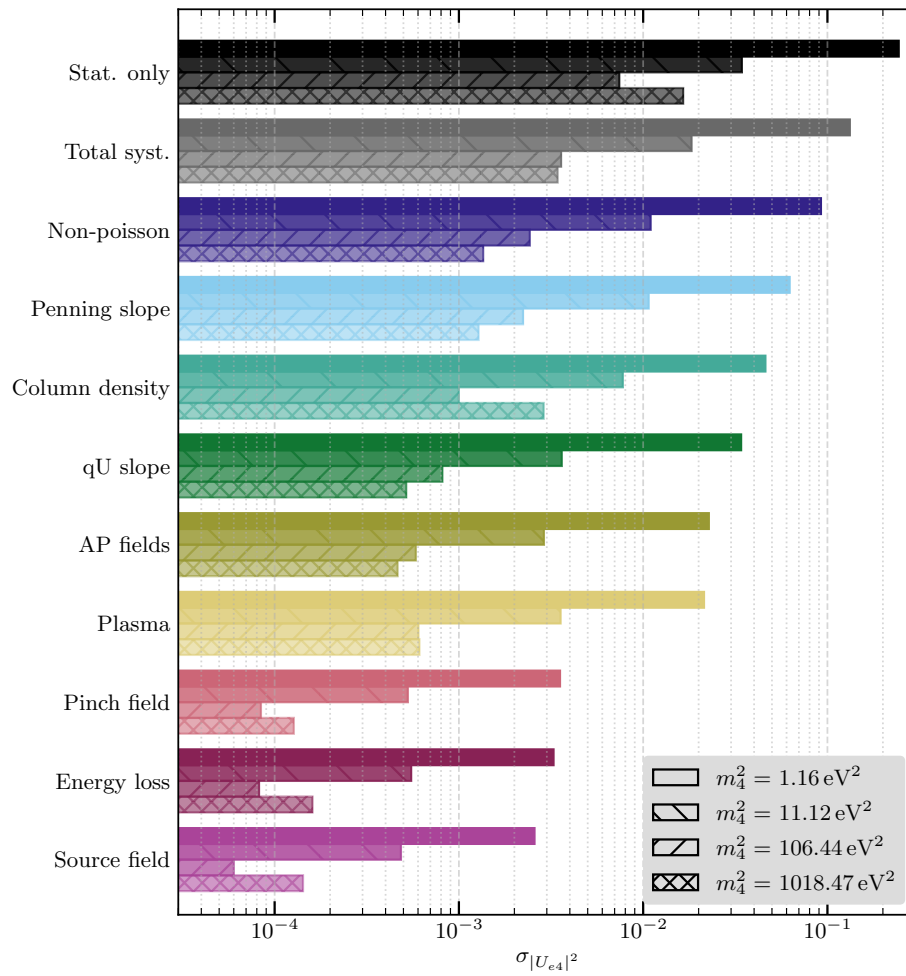


Figure A.4: Impact of individual systematic uncertainties for different values of m_4^2 in KNM-2 obtained from a raster scan.

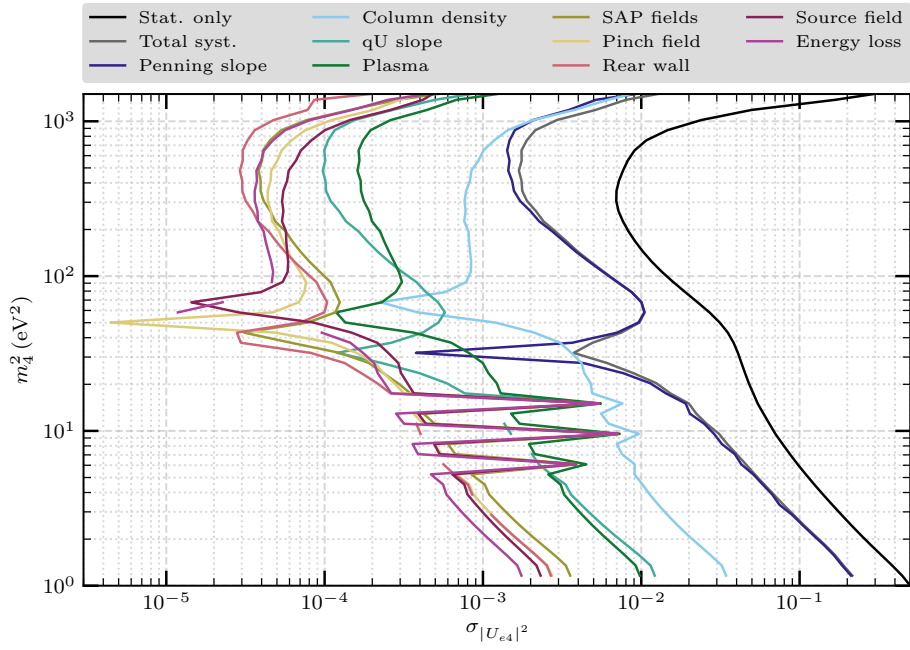


Figure A.5: Impact of individual systematic uncertainties in KNM-3a obtained from a raster scan. The structures visible for masses of about $(5 - 20) \text{ eV}^2$ require further investigation.

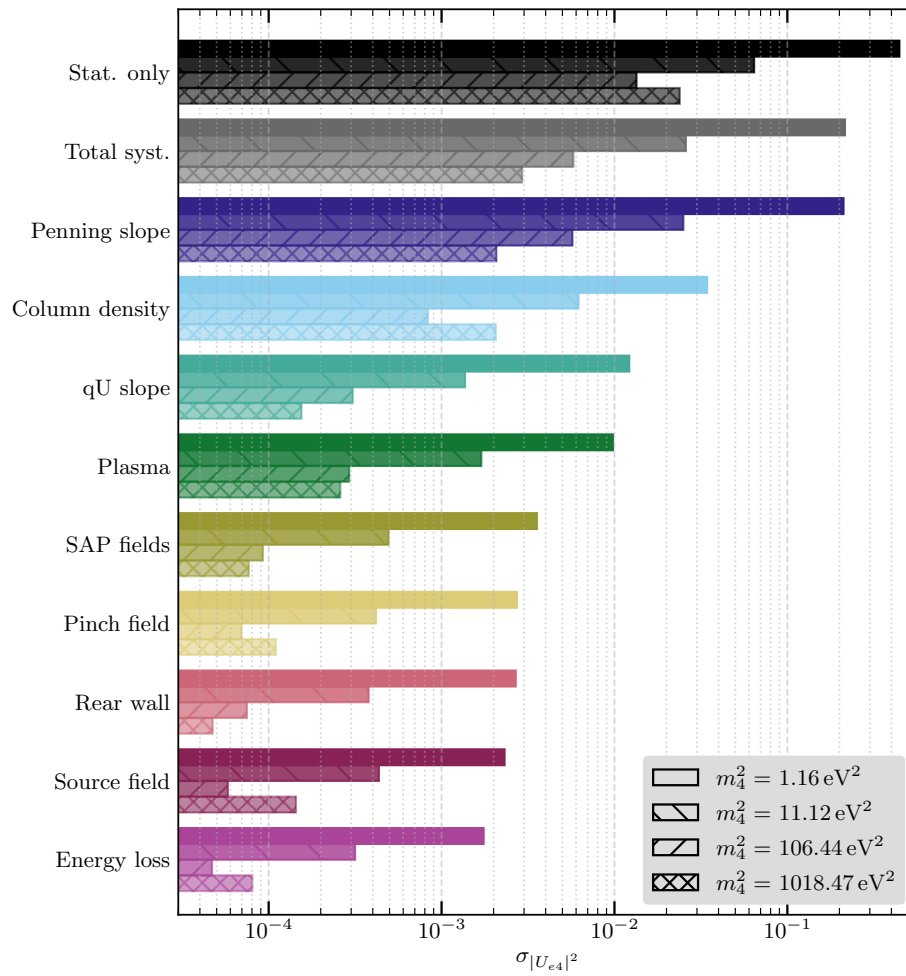


Figure A.6: Impact of individual systematic uncertainties for different values of m_4^2 in KNM-3a obtained from a raster scan.

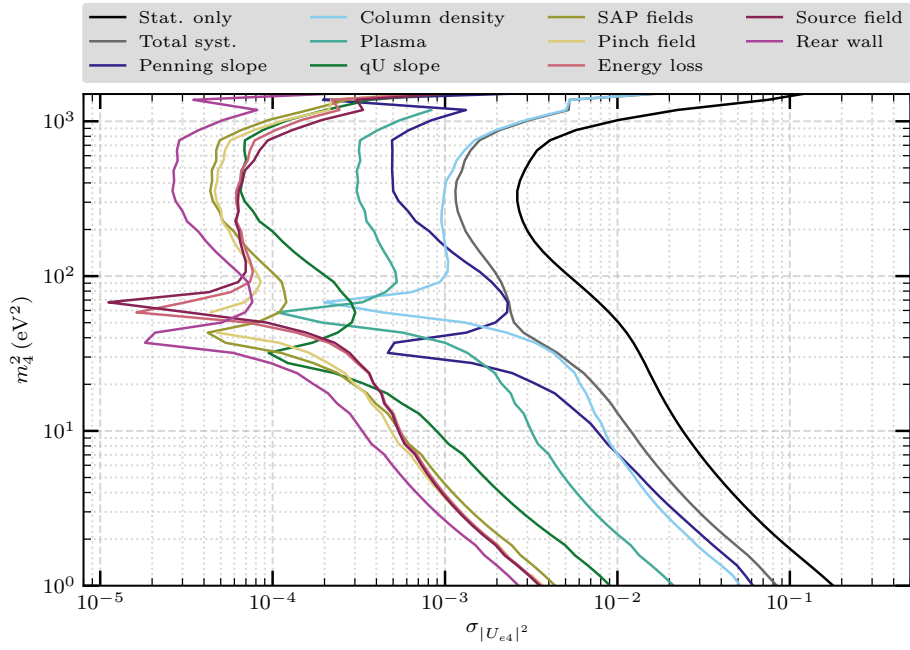


Figure A.7: Impact of individual systematic uncertainties in KNM-4 obtained from a raster scan.

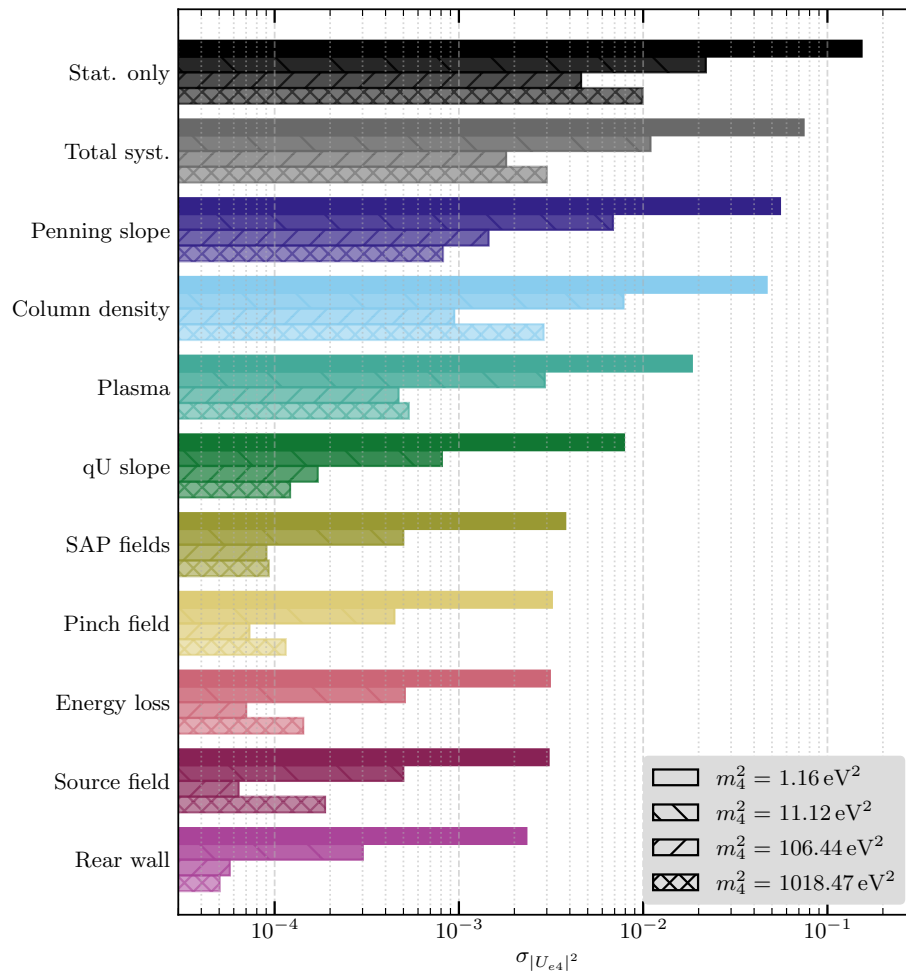


Figure A.8: Impact of individual systematic uncertainties for different values of m_4^2 in KNM-4 obtained from a raster scan.

List of Acronyms

SM standard model of particle physics

PMNS Pontecorvo-Maki-Nakagawa-Sakata

RAA reactor anti-neutrino anomaly

KI National Research Centre Kurchatov Institute

GA gallium anomaly

BEST Baksan Experiment on Sterile Transitions

KATRIN Karlsruhe Tritium Neutrino experiment

TLK Tritium Laboratory Karlsruhe

RS rear section

WGTS windowless gaseous tritium source

DPS differential pumping section

CPS cryogenic pumping section

PS pre-spectrometer

MS main spectrometer

FPD focal plane detector

RW rear wall

e-gun electron gun

TMPs turbo-molecular pumps

MAC-E filter magnetic adiabatic collimation - electrostatic filter

SAP shifted analyzing plane

FSD final state distribution

BED binary-encounter-dipole model

p.d.f. probability density function

List of Figures

1.1	Observed and expected beta decay energy spectrum	2
1.2	Impact of m_ν on the tritium beta spectrum	5
1.3	Impact of a light sterile neutrino on the tritium beta spectrum	7
1.4	Current parameter space for light sterile neutrinos	10
2.1	Overview of the experimental setup of the KATRIN experiment	12
2.2	Working principle of the MAC-E filter	13
2.3	The focal plane detector (FPD) with 148 pixels	14
2.4	Final state distribution (FSD) of $(^3\text{HeT})^+$	15
2.5	Transmission function and energy loss function for one through four scatterings	16
2.6	Response function	17
3.1	Sketched structure of Netrium	22
3.2	The 14 patches used in the analysis of measurement campaigns in the SAP setting	24
4.1	Comparison of the light sterile neutrino signature in Netrium and Fitrium	26
4.2	Null hypothesis Fitrium and Netrium fit	27
4.3	Fitrium and Netrium fit with sterile parameters	27
4.4	Comparison of the Netrium and Fitrium sensitivity contours for KNM-1	28
4.5	Comparison of the Netrium and Fitrium sensitivity contours for KNM-4	29
5.1	The four different pixel combinations	32
5.2	Impact of the different patch combinations on the sensitivity contours at 95% C.L. for the null hypothesis	33
5.3	Impact of the different patches on the sensitivity contours at 95% C.L. for a sterile neutrino signal	34
5.4	Impact of the different patches on the sensitivity contours at 68.3% C.L. for a sterile neutrino signal	34
5.5	Impact of the different patches on the sensitivity contours at 95% C.L. for a different sterile neutrino signal	35
5.6	Impact of the different patches on the sensitivity contours at 68.3% C.L. for a different sterile neutrino signal	36
6.1	Sensitivity contours for all individual measurement campaigns and the combination of all measurement campaigns including only the statistical uncertainty	38
6.2	Sensitivity contours for all individual measurement campaigns and the combination of all measurement campaigns including all systematic uncertainties	38
6.3	Impact of individual systematic uncertainties on $ U_{e4} ^2$ in KNM-3b	39
6.4	Impact of individual systematic uncertainties for different values of m_4^2 in KNM-3b	40
6.5	Impact of individual systematic uncertainties on $ U_{e4} ^2$ in KNM-5	41
6.6	Impact of individual systematic uncertainties for different values of m_4^2 in KNM-5	42
6.7	Sensitivity of KNM-123ab45 in comparison with other experiments	43
6.8	Comparison of sensitivity contours with different fit ranges	45

A.1	Impact of individual systematic uncertainties in KNM-1	49
A.2	Impact of individual systematic uncertainties for different values of m_4^2 in KNM-1 .	50
A.3	Impact of individual systematic uncertainties in KNM-2	51
A.4	Impact of individual systematic uncertainties for different values of m_4^2 in KNM-2 .	52
A.5	Impact of individual systematic uncertainties in KNM-3a	53
A.6	Impact of individual systematic uncertainties for different values of m_4^2 in KNM-3a	54
A.7	Impact of individual systematic uncertainties in KNM-4	55
A.8	Impact of individual systematic uncertainties for different values of m_4^2 in KNM-4 .	56

List of Tables

6.1	Number of electrons in different fit ranges for all measurement campaigns and the combination of all campaigns	37
-----	--	----

Bibliography

- [1] W. Pauli. *Pauli letter collection: letter to Lise Meitner*. 1930. URL: <https://cds.cern.ch/record/83282>.
- [2] C. L. Cowan et al. “Detection of the Free Neutrino: a Confirmation”. In: *Science* 124.3212 (1956). DOI: 10.1126/science.124.3212.103. eprint: <https://www.science.org/doi/pdf/10.1126/science.124.3212.103>.
- [3] G. Danby et al. “Observation of High-Energy Neutrino Reactions and the Existence of Two Kinds of Neutrinos”. In: *Phys. Rev. Lett.* 9 (1962). DOI: 10.1103/PhysRevLett.9.36.
- [4] K. Kodama et al. “Observation of tau neutrino interactions”. In: *Phys. Lett. B* 504 (2001). DOI: 10.1016/S0370-2693(01)00307-0. arXiv: hep-ex/0012035.
- [5] B. Povh et al. *Particles and nuclei*. 2015. URL: <https://link.springer.com/book/10.1007/978-3-662-46321-5>.
- [6] Raymond Davis, Don S. Harmer, and Kenneth C. Hoffman. “Search for Neutrinos from the Sun”. In: *Phys. Rev. Lett.* 20 (21 May 1968). DOI: 10.1103/PhysRevLett.20.1205. URL: <https://link.aps.org/doi/10.1103/PhysRevLett.20.1205>.
- [7] B. Pontecorvo. “Inverse beta processes and nonconservation of lepton charge”. In: *Sov. Phys. JETP* 7 (1958).
- [8] Ziro Maki, Masami Nakagawa, and Shoichi Sakata. “Remarks on the unified model of elementary particles”. In: *Prog. Theor. Phys.* 28 (1962). DOI: 10.1143/PTP.28.870.
- [9] B. Pontecorvo. “Neutrino Experiments and the Problem of Conservation of Leptonic Charge”. In: *Sov. Phys. JETP* 26 (1968).
- [10] L. Oberauer. *Neutrino physics*. 2019. URL: <https://link.springer.com/book/10.1007/978-3-662-59335-6>.
- [11] F. Deppisch. *A Modern Introduction to Neutrino Physics*. 2019. ISBN: 978-1-64327-680-9. DOI: 10.1088/2053-2571/ab21c9. URL: <https://dx.doi.org/10.1088/2053-2571/ab21c9>.
- [12] Y. Fukuda et al. “Evidence for oscillation of atmospheric neutrinos”. In: *Phys. Rev. Lett.* 81 (1998). DOI: 10.1103/PhysRevLett.81.1562. arXiv: hep-ex/9807003.
- [13] Q. R. et al. Ahmad. “Measurement of the Rate of $\nu_e + d \rightarrow p + p + e^-$ Interactions Produced by 8B Solar Neutrinos at the Sudbury Neutrino Observatory”. In: *Phys. Rev. Lett.* 87 (7 July 2001). DOI: 10.1103/PhysRevLett.87.071301. URL: <https://link.aps.org/doi/10.1103/PhysRevLett.87.071301>.
- [14] Q. R. Ahmad et al. “Direct evidence for neutrino flavor transformation from neutral current interactions in the Sudbury Neutrino Observatory”. In: *Phys. Rev. Lett.* 89 (2002). DOI: 10.1103/PhysRevLett.89.011301. arXiv: nucl-ex/0204008.
- [15] M. Aker et al. “Direct neutrino-mass measurement with sub-electronvolt sensitivity”. In: *Nature Phys.* 18.2 (2022). DOI: 10.1038/s41567-021-01463-1. arXiv: 2105.08533 [hep-ex].
- [16] Julien Lesgourgues and Sergio Pastor. “Neutrino mass from Cosmology”. In: *Adv. High Energy Phys.* 2012 (2012). DOI: 10.1155/2012/608515. arXiv: 1212.6154 [hep-ph].

- [17] R. L. Workman. “Review of Particle Physics”. In: *PTEP* 2022 (2022). DOI: 10.1093/ptep/ptac097.
- [18] Steven R. Elliott and Petr Vogel. “Double beta decay”. In: *Ann. Rev. Nucl. Part. Sci.* 52 (2002). DOI: 10.1146/annurev.nucl.52.050102.090641. arXiv: hep-ph/0202264.
- [19] Andrea Giuliani and Alfredo Poves. “Neutrinoless Double-Beta Decay”. In: *Adv. High Energy Phys.* 2012 (2012). DOI: 10.1155/2012/857016.
- [20] M. Agostini et al. “Final Results of GERDA on the Search for Neutrinoless Double- β Decay”. In: *Phys. Rev. Lett.* 125.25 (2020). DOI: 10.1103/PhysRevLett.125.252502. arXiv: 2009.06079 [nucl-ex].
- [21] S. Abe et al. “First Search for the Majorana Nature of Neutrinos in the Inverted Mass Ordering Region with KamLAND-Zen”. In: (Mar. 2022). arXiv: 2203.02139 [hep-ex].
- [22] E. W. Otten and C. Weinheimer. “Neutrino mass limit from tritium β decay”. In: *Reports on Progress in Physics* 71.8 (July 2008). DOI: 10.1088/0034-4885/71/8/086201. URL: <https://doi.org/10.1088/0034-4885/71/8/086201>.
- [23] Christian Weinheimer. “Laboratory Limits on Neutrino Masses”. In: *Neutrino Mass*. Ed. by Klaus Winter and Guido Altarelli. Berlin, Heidelberg: Springer Berlin Heidelberg, 2003. ISBN: 978-3-540-44901-0. DOI: 10.1007/978-3-540-44901-0_2. URL: https://doi.org/10.1007/978-3-540-44901-0_2.
- [24] M. Kleesiek et al. “ β -Decay Spectrum, Response Function and Statistical Model for Neutrino Mass Measurements with the KATRIN Experiment”. In: *Eur. Phys. J. C* 79.3 (2019). DOI: 10.1140/epjc/s10052-019-6686-7. arXiv: 1806.00369 [physics.data-an].
- [25] Sebastian Böser et al. “Status of Light Sterile Neutrino Searches”. In: *Prog. Part. Nucl. Phys.* 111 (2020). DOI: 10.1016/j.pnpnp.2019.103736. arXiv: 1906.01739 [hep-ex].
- [26] K. N. Abazajian et al. “Light Sterile Neutrinos: A White Paper”. In: (Apr. 2012). arXiv: 1204.5379 [hep-ph].
- [27] W. Hampel et al. “Final results of the Cr-51 neutrino source experiments in GALLEX”. In: *Phys. Lett. B* 420 (1998). DOI: 10.1016/S0370-2693(97)01562-1.
- [28] J. N. Abdurashitov et al. “Measurement of the solar neutrino capture rate with gallium metal. III: Results for the 2002–2007 data-taking period”. In: *Phys. Rev. C* 80 (2009). DOI: 10.1103/PhysRevC.80.015807. arXiv: 0901.2200 [nucl-ex].
- [29] S. Gariazzo et al. “Light sterile neutrinos”. In: *J. Phys. G* 43 (2016). DOI: 10.1088/0954-3899/43/3/033001. arXiv: 1507.08204 [hep-ph].
- [30] V. V. Barinov et al. “Results from the Baksan Experiment on Sterile Transitions (BEST)”. In: *Phys. Rev. Lett.* 128.23 (2022). DOI: 10.1103/PhysRevLett.128.232501. arXiv: 2109.11482 [nucl-ex].
- [31] C. Giunti et al. “Gallium Anomaly: Critical View from the Global Picture of ν_e and $\bar{\nu}_e$ Disappearance”. In: (Sept. 2022). arXiv: 2209.00916 [hep-ph].
- [32] Th. A. Mueller et al. “Improved Predictions of Reactor Antineutrino Spectra”. In: *Phys. Rev. C* 83 (2011). DOI: 10.1103/PhysRevC.83.054615. arXiv: 1101.2663 [hep-ex].
- [33] G. Mention et al. “The Reactor Antineutrino Anomaly”. In: *Phys. Rev. D* 83 (2011). DOI: 10.1103/PhysRevD.83.073006. arXiv: 1101.2755 [hep-ex].
- [34] C. Giunti et al. “Reactor antineutrino anomaly in light of recent flux model refinements”. In: *Phys. Lett. B* 829 (2022). DOI: 10.1016/j.physletb.2022.137054. arXiv: 2110.06820 [hep-ph].
- [35] M. Estienne et al. “Updated Summation Model: An Improved Agreement with the Daya Bay Antineutrino Fluxes”. In: *Phys. Rev. Lett.* 123.2 (2019). DOI: 10.1103/PhysRevLett.123.022502. arXiv: 1904.09358 [nucl-ex].

-
- [36] V. Kopeikin, M. Skorokhvatov, and O. Titov. “Reevaluating reactor antineutrino spectra with new measurements of the ratio between U235 and Pu239 β spectra”. In: *Phys. Rev. D* 104.7 (2021). DOI: 10.1103/PhysRevD.104.L071301. arXiv: 2103.01684 [nucl-ex].
- [37] Jeffrey M. Berryman and Patrick Huber. “Sterile Neutrinos and the Global Reactor Antineutrino Dataset”. In: *JHEP* 01 (2021). DOI: 10.1007/JHEP01(2021)167. arXiv: 2005.01756 [hep-ph].
- [38] A. P. Serebrov et al. “Search for sterile neutrinos with the Neutrino-4 experiment and measurement results”. In: *Phys. Rev. D* 104.3 (2021). DOI: 10.1103/PhysRevD.104.032003. arXiv: 2005.05301 [hep-ex].
- [39] C. Giunti et al. “Neutrino-4 anomaly: oscillations or fluctuations?” In: *Phys. Lett. B* 816 (2021). DOI: 10.1016/j.physletb.2021.136214. arXiv: 2101.06785 [hep-ph].
- [40] M. V. Danilov and N. A. Skrobova. “Comment on “Analysis of the Results of the Neutrino-4 Experiment on the Search for the Sterile Neutrino and Comparison with Results of Other Experiments” (JETP Letters 112, 199 (2020))”. In: *JETP Lett.* 112.7 (2020). DOI: 10.1134/S0021364020190066.
- [41] Igor Genadievich Alekseev and Nataliya Skrobova. “Recent results of the DANSS experiment”. In: *PoS NuFact2021* (2022). DOI: 10.22323/1.402.0143.
- [42] M. Andriamirado et al. “Improved short-baseline neutrino oscillation search and energy spectrum measurement with the PROSPECT experiment at HFIR”. In: *Phys. Rev. D* 103.3 (2021). DOI: 10.1103/PhysRevD.103.032001. arXiv: 2006.11210 [hep-ex].
- [43] H. Almazán et al. “Improved sterile neutrino constraints from the STEREO experiment with 179 days of reactor-on data”. In: *Phys. Rev. D* 102.5 (2020). DOI: 10.1103/PhysRevD.102.052002. arXiv: 1912.06582 [hep-ex].
- [44] Ch. Kraus et al. “Final results from phase II of the Mainz neutrino mass search in tritium beta decay”. In: *Eur. Phys. J. C* 40 (2005). DOI: 10.1140/epjc/s2005-02139-7. arXiv: hep-ex/0412056.
- [45] V. N. Aseev et al. “An upper limit on electron antineutrino mass from Troitsk experiment”. In: *Phys. Rev. D* 84 (2011). DOI: 10.1103/PhysRevD.84.112003. arXiv: 1108.5034 [hep-ex].
- [46] J. Angrik et al. “KATRIN design report 2004”. In: (Feb. 2005).
- [47] Martin Babutzka. “Design and development for the Rearsection of the KATRIN experiment”. PhD thesis. 2014.
- [48] M. Aker et al. “Precision measurement of the electron energy-loss function in tritium and deuterium gas for the KATRIN experiment”. In: *Eur. Phys. J. C* 81.7 (2021). DOI: 10.1140/epjc/s10052-021-09325-z. arXiv: 2105.06930 [physics.ins-det].
- [49] J. Behrens et al. “A pulsed, mono-energetic and angular-selective UV photo-electron source for the commissioning of the KATRIN experiment”. In: *Eur. Phys. J. C* 77.6 (2017). DOI: 10.1140/epjc/s10052-017-4972-9. arXiv: 1703.05272 [physics.ins-det].
- [50] Florian Heizmann and Hendrik Seitz-Moskaliuk. “The Windowless Gaseous Tritium Source (WGTS) of the KATRIN experiment”. In: *J. Phys. Conf. Ser.* 888.1 (2017). DOI: 10.1088/1742-6596/888/1/012071.
- [51] S. Lukic et al. “Measurement of the gas-flow reduction factor of the KATRIN DPS2-F differential pumping section”. In: *Vacuum* 86 (2012). DOI: 10.1016/j.vacuum.2011.10.017. arXiv: 1107.0220 [physics.ins-det].
- [52] Woosik Gil et al. “The Cryogenic Pumping Section of the KATRIN Experiment”. In: *IEEE Trans. Appl. Supercond.* 20.3 (2009). DOI: 10.1109/TASC.2009.2038581.
- [53] Carsten Röttele. “Results of the first Cool-down of the KATRIN Cryogenic Pumping Section”. In: *J. Phys. Conf. Ser.* 888.1 (2017). DOI: 10.1088/1742-6596/888/1/012228.
-

- [54] Christian Karl. “First Sub-Electronvolt Direct Neutrino Mass Measurement with the KATRIN Experiment”. PhD thesis. 2022.
- [55] M. Aker et al. “The design, construction, and commissioning of the KATRIN experiment”. In: *JINST* 16.08 (2021). DOI: 10.1088/1748-0221/16/08/T08015. arXiv: 2103.04755 [physics.ins-det].
- [56] Florian M. Fränkle et al. “Penning discharge in the KATRIN pre-spectrometer”. In: *JINST* 9 (2014). DOI: 10.1088/1748-0221/9/07/P07028.
- [57] Alexey Lokhov et al. “Background reduction at the KATRIN experiment by the shifted analysing plane configuration”. In: *Eur. Phys. J. C* 82.3 (2022). DOI: 10.1140/epjc/s10052-022-10220-4. arXiv: 2201.11743 [physics.ins-det].
- [58] J. F. Amsbaugh et al. “Focal-plane detector system for the KATRIN experiment”. In: *Nucl. Instrum. Meth. A* 778 (2015). DOI: 10.1016/j.nima.2014.12.116. arXiv: 1404.2925 [physics.ins-det].
- [59] Stefan Groh. “Modeling of the response function and measurement of transmission properties of the KATRIN experiment”. PhD thesis. KIT, Karlsruhe, Dept. Phys., 2015. DOI: 10.5445/IR/1000046546.
- [60] Matthias Weidenthaler. *Systematic Uncertainties of the KATRIN Neutrino Mass Measurement Associated with Beta Decays on the Rear Wall of the Experiment*. 2022.
- [61] Moritz Machatschek. “A Phenomenological Theory of KATRIN Source Potential Systematics and its Application in Krypton-83m Calibration Measurements”. PhD thesis. 2020.
- [62] Anna Stadler. “Characterization and mitigation of the background in KATRIN”. PhD thesis. 2020.
- [63] A. Saenz et al. *Fitter Input: Molecular Final State Distribution*. KATRIN Internal. 2021. URL: https://ikp-katrin-wiki.ikp.kit.edu/katrin/images/b/b2/Katrin_cm41_fsd.pdf.
- [64] Christoph Wiesinger. *Detector systematics in neutrino mass analysis*. KATRIN Internal. 2021. URL: https://ikp-katrin-wiki.ikp.kit.edu/katrin/images/6/6e/20210713_DetectorSystematics_AnalysisCall.pdf.
- [65] Christian Karl. *Analysis of First Tritium Data of the KATRIN Experiment*. 2018.
- [66] Glen Cowan. *Statistical Data Analysis*. Oxford Science Publications, 1998.
- [67] S. S. Wilks. “The Large-Sample Distribution of the Likelihood Ratio for Testing Composite Hypotheses”. In: *The Annals of Mathematical Statistics* 9.1 (1938). DOI: 10.1214/aoms/1177732360. URL: <https://doi.org/10.1214/aoms/1177732360>.
- [68] M. Aker et al. “Improved eV-scale sterile-neutrino constraints from the second KATRIN measurement campaign”. In: *Phys. Rev. D* 105.7 (2022). DOI: 10.1103/PhysRevD.105.072004. arXiv: 2201.11593 [hep-ex].
- [69] Alessandro Schwemmer et al. *KNM1-5 unblinding step 1*. KATRIN Internal. 2022. URL: https://indico.scc.kit.edu/event/2895/contributions/11321/attachments/5447/8381/20220928_KNM123ab45-UB1_CollaborationMeeting.pdf.

Acknowledgements

I would like to thank

- Susanne Mertens for the possibility to work on this exciting topic as well as the constant support;
- Christoph Köhler for his great supervision and support during the course of this thesis;
- Christian Karl, Alessandro Schwemmer and Christoph Wiesinger for their support regarding Fitrium, Netrium and the analysis in general;
- Thierry Lasserre for sharing his vast knowledge about sterile neutrinos and other related topics;
- Everyone who proof-read parts of this thesis;
- Anna Schubert and Pia Voigt for the good vibes in our office;
- All students and members of E47 for the great working environment.

Zuletzt möchte ich mich bei meinen Eltern und bei meiner Freundin für die bedingungslose Unterstützung bedanken, welche das Studium und damit diese Arbeit überhaupt erst ermöglicht haben.